SPARK CHAMBER MEASUREMENT

OF THE Σ^+ LIFETIME

By

LEWIS PORTER KELLER

Bachelor of Science
Valparaiso University
Valparaiso, Indiana
1960

Master of Science
Oklahoma State University
Stillwater, Oklahoma
1962

Submitted to the Faculty of the
Graduate College of the
Oklahoma State University
in partial fulfillment of
the requirements for
the Degree of
DOCTOR OF PHILOSOPHY
May, 1969

SPARK CHAMBER MEASUREMENT

OF THE Σ^+ LIFETIME

Thesis Approved:

Leon W. Schroeder
Thesis Adviser

Robert A Schluter

N. V. V. J. Swamy

John Blakely

D. D. Dunham
Dean of the Graduate College

PREFACE

The nonleptonic decay of the charged sigma hyperons is dominated by the selection rule, $|\Delta I| = 1/2$, where ΔI denotes the change in the total isotopic spin of the initial and final states.

The decay rate of Σ^+ hyperons produced in the reaction $\pi^+ + p \rightarrow \Sigma^+ + K^+$ was measured using a new method: high precision wide gap spark chambers operated in the track mode, from which ionization measurements of the wide gap tracks were used to distinguish the nonleptonic decay modes, $\Sigma^+ \rightarrow p + \pi^o$ or $n + \pi^+$.

I would like to acknowledge the contribution and aid of Dr. Robert Schluter and the advice and encouragement of Dr. Leon Schroeder.

My discussions with Mr. Earl Hoffman have been very helpful in the completion of the experiment.

I want to thank the Argonne National Laboratory for their financial support for the use of their facilities during my years of off-campus research.

This experiment was supported by the Atomic Energy Commission.

TABLE OF CONTENTS

LIST OF TABLES

LIST OF FIGURES

CHAPTER I

INTRODUCTION

An experiment to measure the decay rate of Σ^+ hyperons produced in the reaction $\pi^+ + p \rightarrow \Sigma^+ + K^+$ has been done using high precision wide gap spark chambers operated in the track mode. Using a π^+ beam from the Argonne Zero Gradient Synchrotron positive sigmas were produced in a liquid hydrogen target and detected by requiring the charged particle from either $\Sigma^+ \rightarrow p\,\pi^o$ or $n\,\pi^+$ to be in coincidence with a delayed count in a stopping K^+ Čerenkov counter. The event geometry was reconstructed by projecting the K^+ and decay charged particle tracks back into the target region where there were no detectors. Ionization measurement of the wide gap tracks was used to distinguish the nonleptonic decay modes.

The first reported measurements of the Σ^+ decay rate were done in nuclear emulsion with Σ^+'s produced in the reaction $K^- + p \rightarrow \Sigma^\pm + \pi^\mp$ (1). Since the proton momentum is unknown, the sigma energy had to be determined from the decay kinematics, which can give an accurate result only in the mode $\Sigma^+ \rightarrow p\,\pi^o$.

The emulsion experiments were followed by a series of hydrogen bubble chamber experiments (1), all of which are plagued by the

difficulty of avoiding a scanning bias on the Σ^+ length. This potential bias results in part from the fact that bubble chambers use small angle stereo views to photograph an event, so that depth precision is lost. In addition, bubble chamber experiments which produce Σ's in the reaction $K^- + p \rightarrow \Sigma^{\pm} + \pi^{\pm}$, where the K^- is at rest, can have the following configurations:

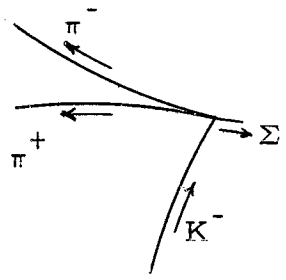

A (charge ambiguous)

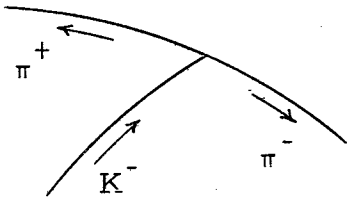

B (colinear decay)

In configuration A the sigma charge cannot be determined, while in B both the charge and length are unknown. Events of these types cannot be ignored since the ambiguity arises more often for short Σ's than for long ones.

The present experiment was designed to trigger the recording device (optical wide gap spark chamber) with an efficiency independent of the Σ^+ length. The method of selecting recorded events for measurement was also designed to be free of a length bias. The sigma

momentum was ambiguously determined by production in liquid hydrogen, which was not the case in the only previous spark chamber measurement of the Σ^+ lifetime (1). Finally, the Σ^+ length was reconstructed using wide gap spark chambers, which are known to be more precise than conventional sampling spark chambers.

CHAPTER II

THE EXPERIMENT

Beam

The experiment was performed in a π^+ beam originating in a beryllium target placed in the external proton beam at the Argonne ZGS. The beam layout is shown in Figure 1 and the beam parameters are listed in Table I. The particle momentum was selected by bending magnet B1, and the beam was horizontally focused at the momentum slit with a magnification of - 0.8 by quadrupole magnets Q1 and Q2. The momentum dispersion at the slit was 1.27 cm for a 1 % $\Delta P/P$, so that for a slit of full width 2.54 cm the solid angle for particles with momenta ± 1% from the central momentum was reduced by 1/2. The fields in the second quadrupole doublet, Q3 and Q4, were set to give a nominally parallel beam at the experimental apparatus. The absolute value of the central momentum was measured to an accuracy of ± .2% before and after the experiment with a floating wire stretched between the production target position and hydrogen target. The beam size was determined by a 60 cm long lead collimator following Q4, while the angular spread was due mainly to multiple coulomb

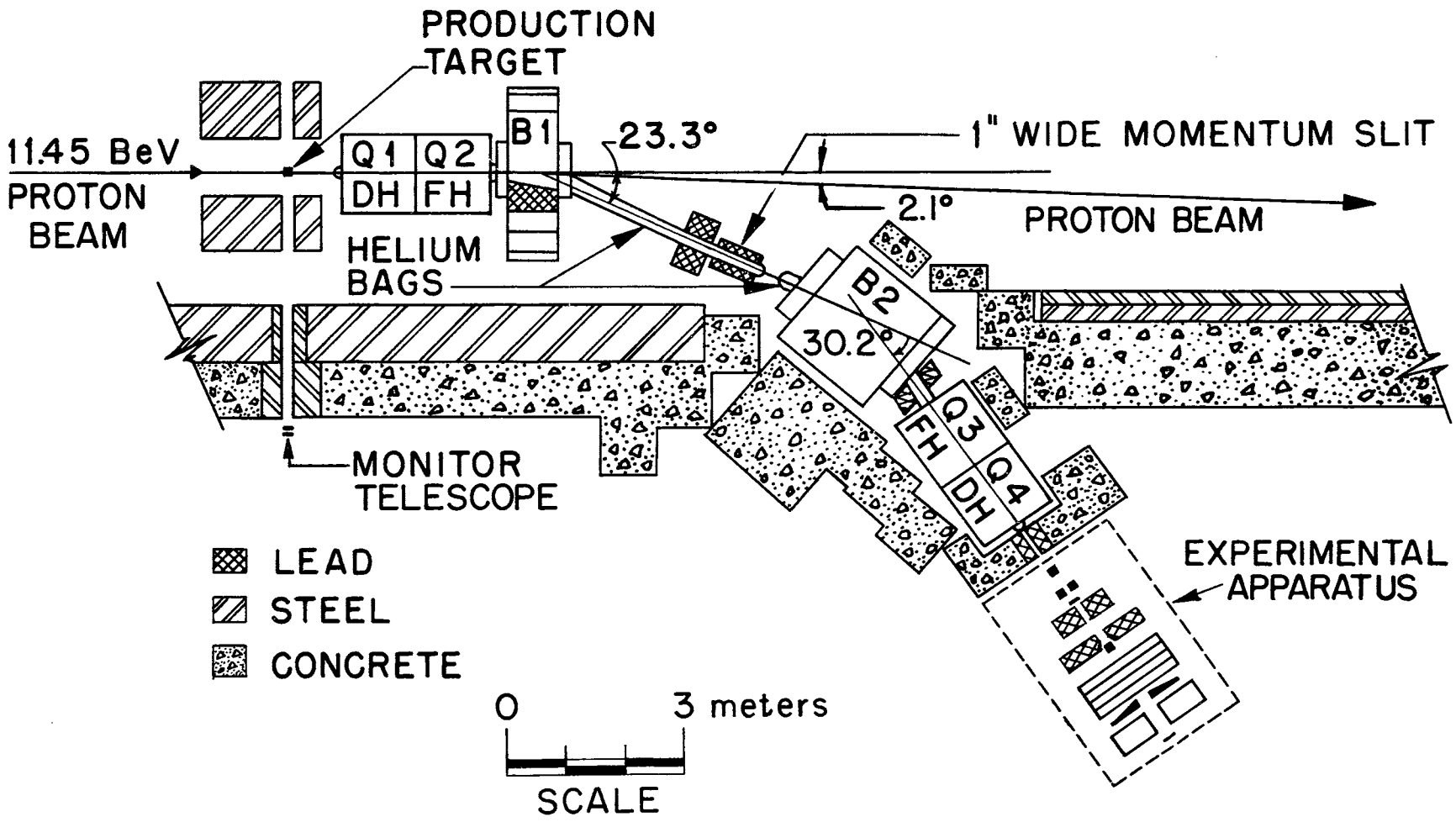

Figure 1. Beam Layout

TABLE I

BEAM PARAMETERS

Length	15.9 meters
Solid Angle	5.0×10^{-4} ster. (calculated)
Momentum Spread	$\pm$1.0% (calculated)
Divergence	
a) horizontal	8 mrad (measured)
b) vertical	9 mrad "
Size	
a) horizontal	2.7 cm (measured)
b) vertical	3.2 cm "
Rate	20,000/pulse (measured average of all particles giving beam trigger)
Contamination of Other Particles in Beam Counters	
a) protons	<10% (estimated from oscilloscope study)
b) positrons	38% (Reference 2)
c) muons	<1% (calculated)

scattering in the pion beam counter. Figure 2 shows the beam profile and distribution of slopes determined by triggering the spark chambers with beam particles. This was done several times during the run.

Figure 3 shows a plan view of the experimental apparatus. The remainder of this chapter will be devoted to a description of the various parts of the apparatus.

Beam Counters

Beam pions were selected with a Čerenkov counter labeled P on Figure 3. Figure 4 shows a drawing of the counter which consisted simply of a plexiglas (acrylic) radiator optically coupled to the photocathode of a fast RCA C70045D photomultiplier tube. The surfaces of the radiator were blackened and the counter oriented so that some pion light ($\check{C}$ angle = 47.9^{o}, $N_{\gamma\pi}$ = 290 γ's/cm) impinged directly on the photocathode while most proton radiated light ($\check{C}$ angle = 30^{o}, $N_{\gamma p}$ = 140 γ's/cm) was absorbed at the surface of the radiator. Pion light emitted away from the photocathode is also absorbed to keep the time spread of incident photons as small as possible. The phototube was followed by a discriminator with a variable passive attenuator at the input. The attenuator was set so that pion pulses triggered the discriminator circuit while the smaller proton pulses were rejected. The final beam signal was obtained by requiring a coincidence between P and a 2-1/2" diameter, 1/8" thick scintillator, A, which assured that the beam

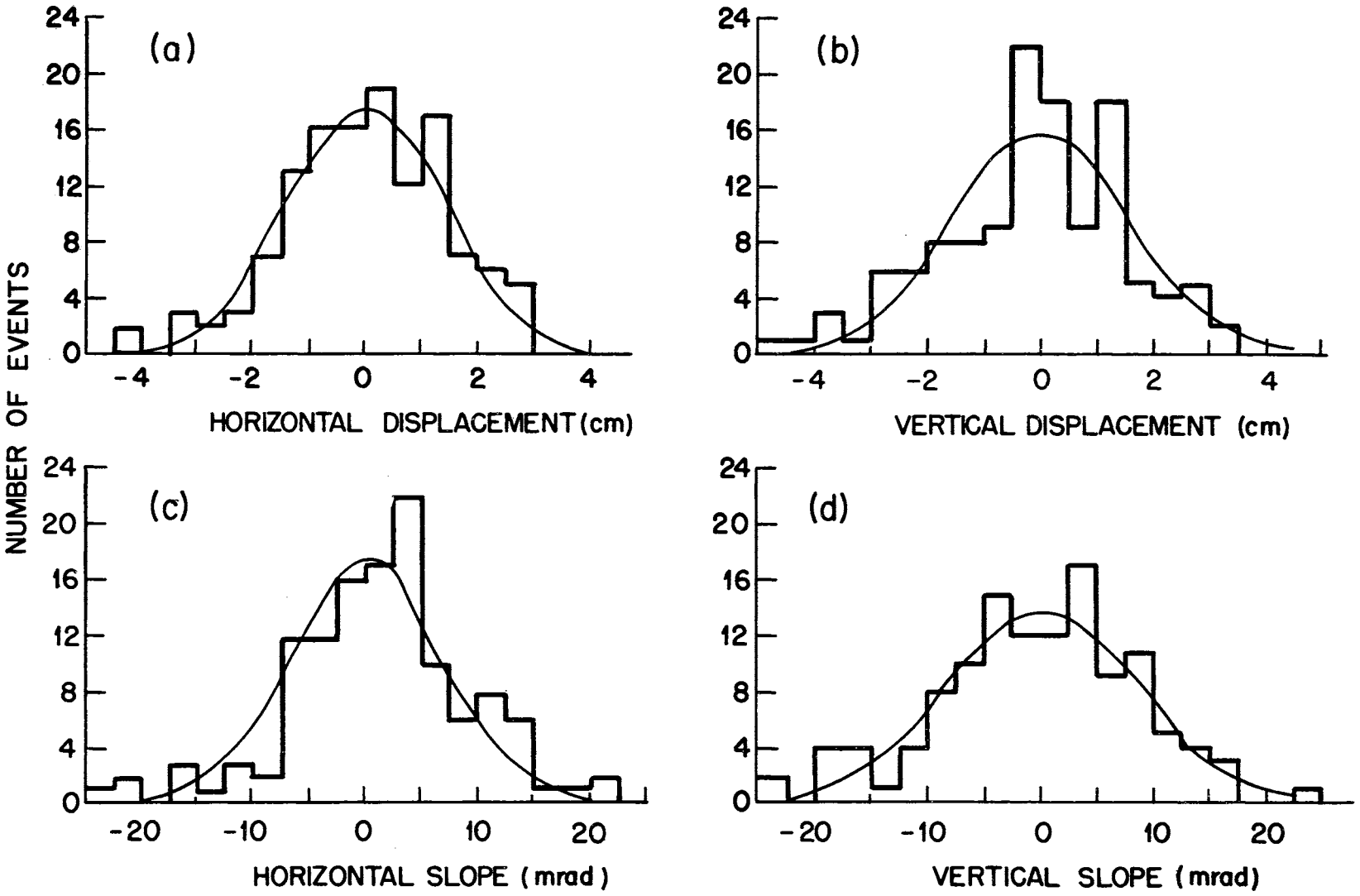

Figure 2. Spatial and Angular Distribution of the Beam

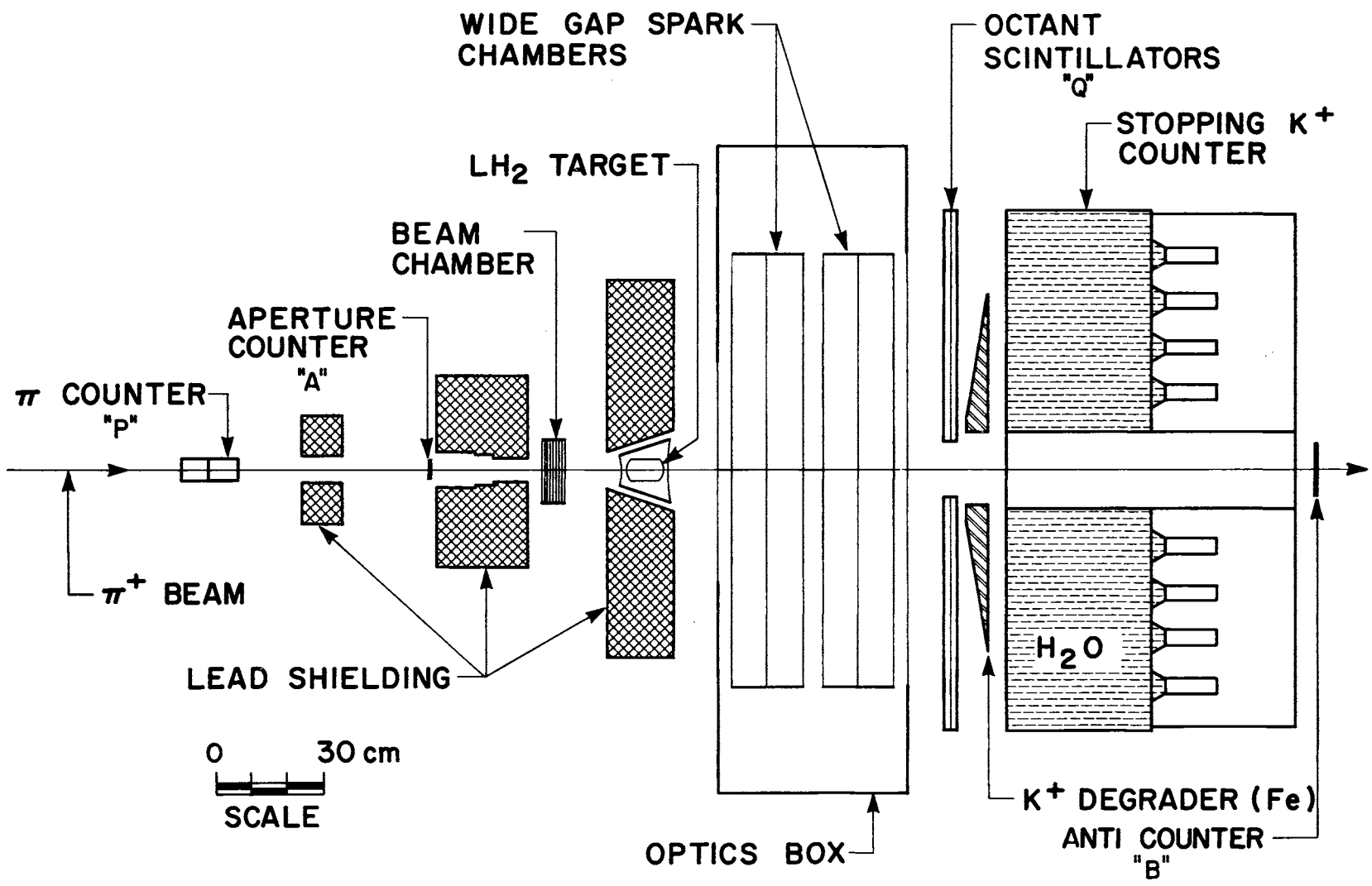

Figure 3. Plan View of the Experimental Apparatus

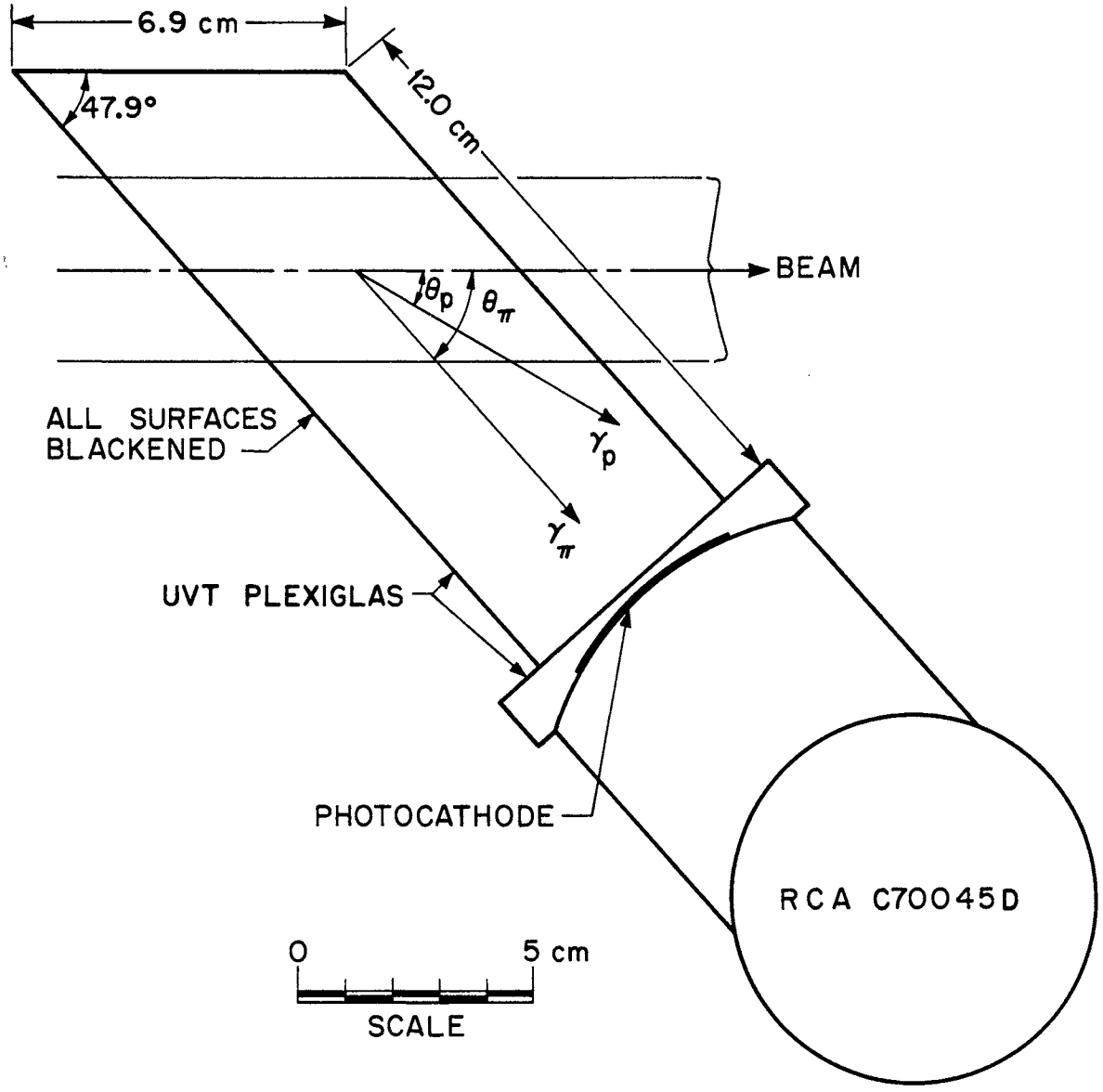

Figure 4. Pion Cerenkov Counter

particle passed through the lead collimator hole (Figure 3). To keep a continuous monitor of the pion counter gain, a fanned signal from the PA coincidence circuit triggered the sweep of an oscillosope whose input contained pulses from a scintillator (labeled B in Figure 3) located 3 m downstream from the pion counter (time separation between pions and protons over this distance $\simeq 3$ nsec); so that most sweeps contained a pion pulse while $< 10\%$ (estimated) of sweeps contained a proton pulse ~ 3 nsec later than the pion signal.

Liquid Hydrogen Target

The pion beam impinged on a liquid hydrogen target which was approximately a right cylinder of volume 250 cc and of mean length 8 cm along the beam axis (Figure 5). The target flask was constructed of mylar with nominal thickness 0.125 mm and was wrapped with 5 layers of NRC-2 superinsulation (3). The vacuum jacket windows were mylar of 0.125 and 0.250 mm nominal thickness. These windows were also covered externally by several layers of superinsulation. The target assembly presented to the beam a total of 556 mg/cm^2 of liquid hydrogen and about 100 mg/cm^2 of mylar. The probability that a pion will interact in the liquid hydrogen was 3.4×10^{-7} per microbarn of interaction cross section. The hydrogen was liquified with a mechanical helium refrigerator now in standard use at Argonne (4).

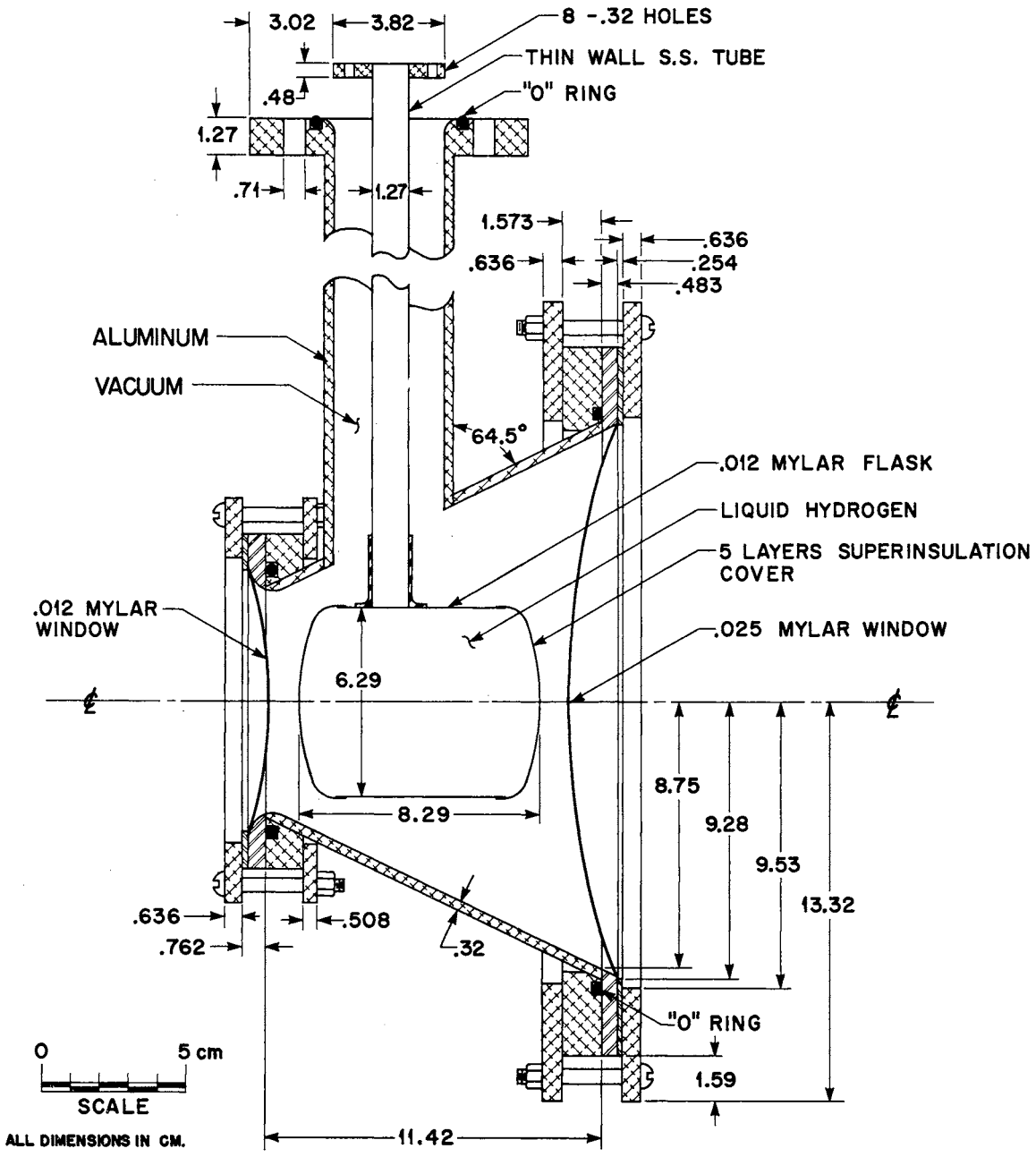

Figure 5. Liquid Hydrogen Target

Wide Gap Spark Chamber System

The operational characteristics of wide gap spark chambers similar to those used in this experiment are described elsewhere (5). The spark chamber consisted of 2 modules, 1 of which is shown in Figure 6. The modules were identical except for the plate material. The chamber closest to the liquid hydrogen target had plates of 25 μ stainless steel foil and the downstream chamber plates were 25 μ aluminum foil.

A module consisted of 3 aluminum frames of thickness 1.27 cm with outside dimensions 1.32 m by 1.32 m and inside dimensions 1.22 m by 1.22 m with corners of 30 cm radius. A 0.125 mm relief 4.4 cm wide for epoxy was milled in the frames on the side to receive the metal foil.

The foils were stretched until wrinkle free on an oversized square frame. The chamber frame relief was coated with epoxy, raised against the foil, and held until the epoxy had cured. Figure 6 shows the arrangement of the foils on the frames. The outside of the 2 outer frames was covered with a 25 μ mylar film to provide equal pressure on all sides of the metal foils. Another plastic film of 25 μ teflon covered the mylar to prevent diffusion of water vapor into the chambers. The spaces on both sides of each metal foil were interconnected with external tygon tubing so that there would be no pressure differential

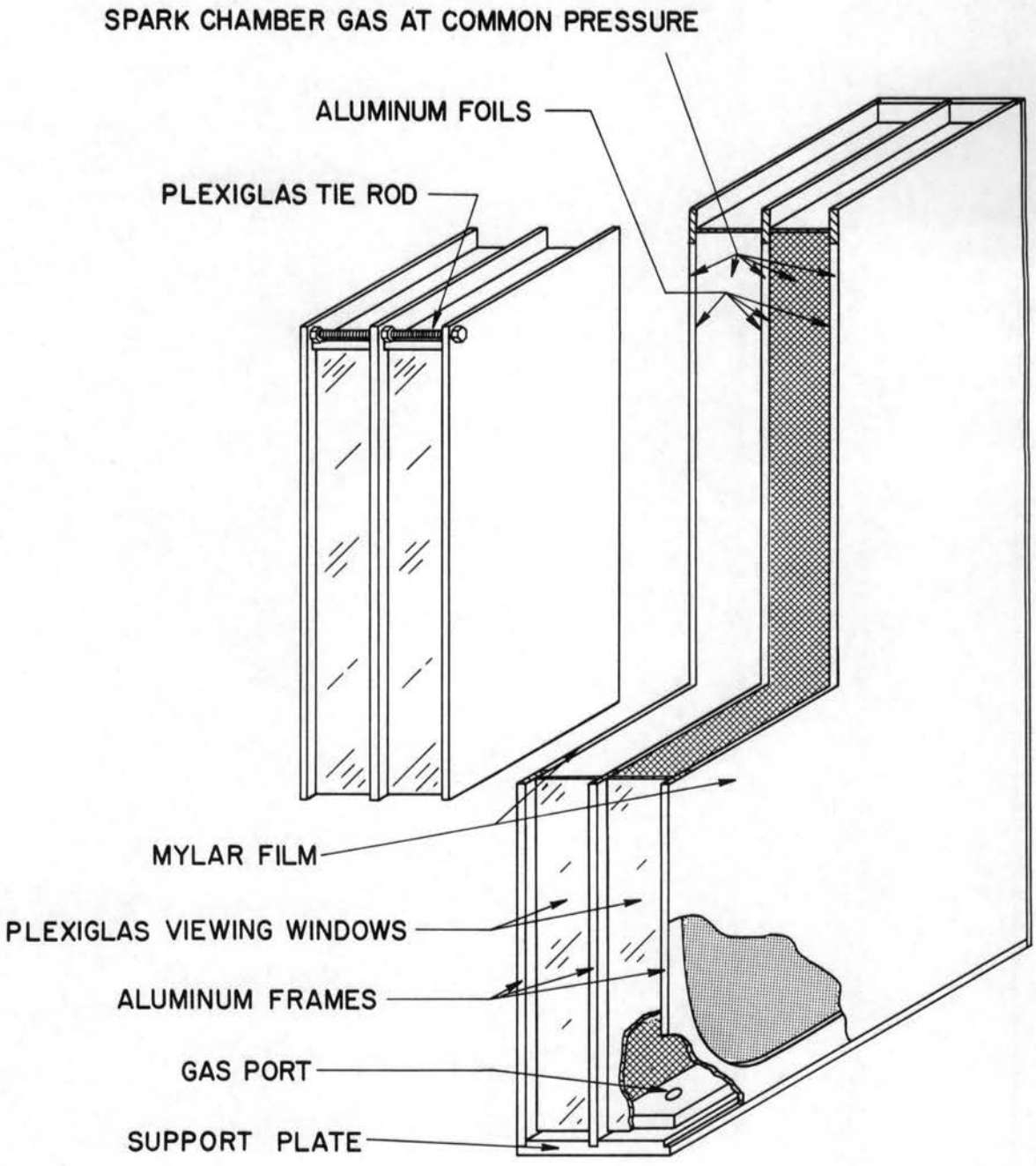

Figure 6. Spark Chamber Module

across them. The chambers were operated at a pressure slightly above atmosphere so that in case of small leaks, air did not leak in.

The frames were held 10.02 cm apart by plexiglas windows which were recessed 3.8 cm from the outer edge of the frames. This placement was to prevent spontaneous electrical breakdown in the spark chamber gas due to the higher electric field at the edges and corners of the frames. Two adjacent windows were 1.6 mm thick for viewing with minimum distortion. The other 2 spacers were 2.5 cm plexiglas with the inside surface frosted to prevent reflections. The plexiglas to frame seals were made with General Electric Silicone Rubber RTV 102. Two 2.5 cm micarta support plates opposite the viewing windows gave the assembly strength. An aluminum mounting plate (not shown in Figure 6) was attached to the micarta plate to provide a location for gas gauges and tubing and to facilitate handling.

A block diagram of the spark chamber electronics is shown in Figure 7. The mechanical properties of the Marx high voltage pulse generator (6) are shown in Figure 8, and Figure 9 shows the Marx generator electronics with various rf shielding elements and the spark chamber load. The series R-L-C circuit in parallel with the spark chamber was chosen to critically damp the high voltage pulse.

The Marx generator and spark chambers were surrounded by copper and aluminum boxes to provide electromagnetic radiation shielding. All leads entering or leaving these boxes were isolated with inductors to limit the rf noise escaping.

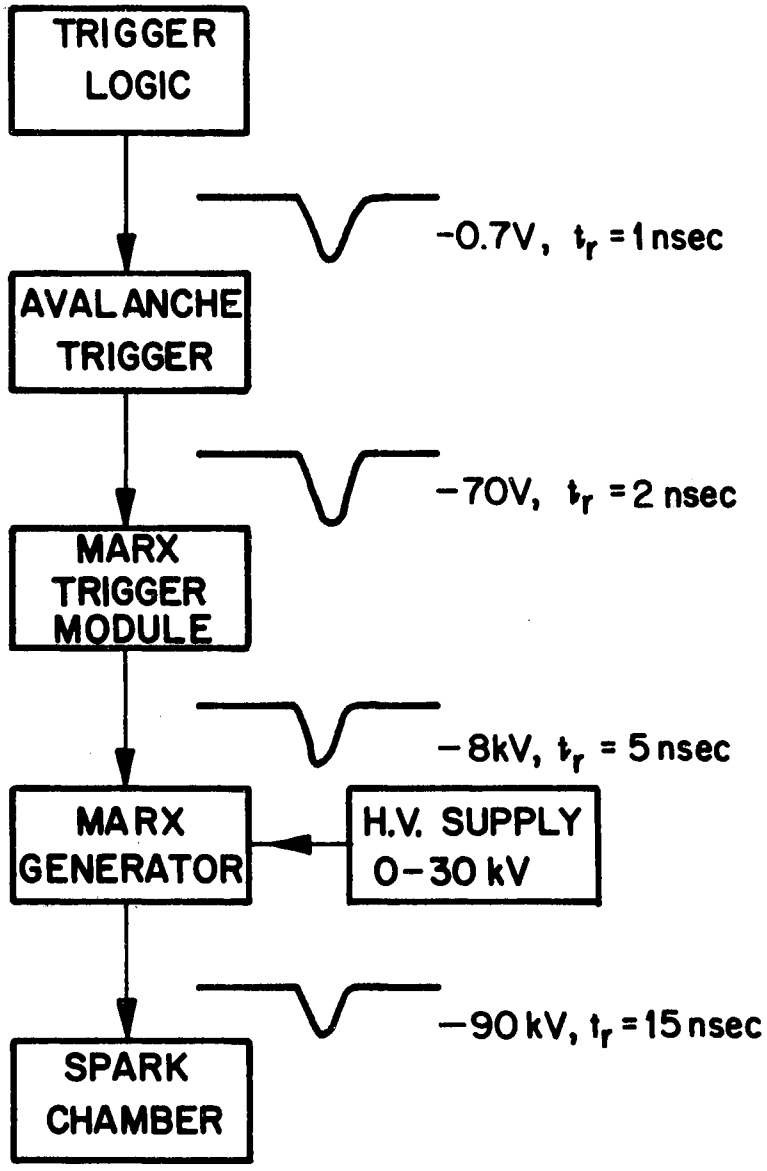

Figure 7. Spark Chamber Electronics

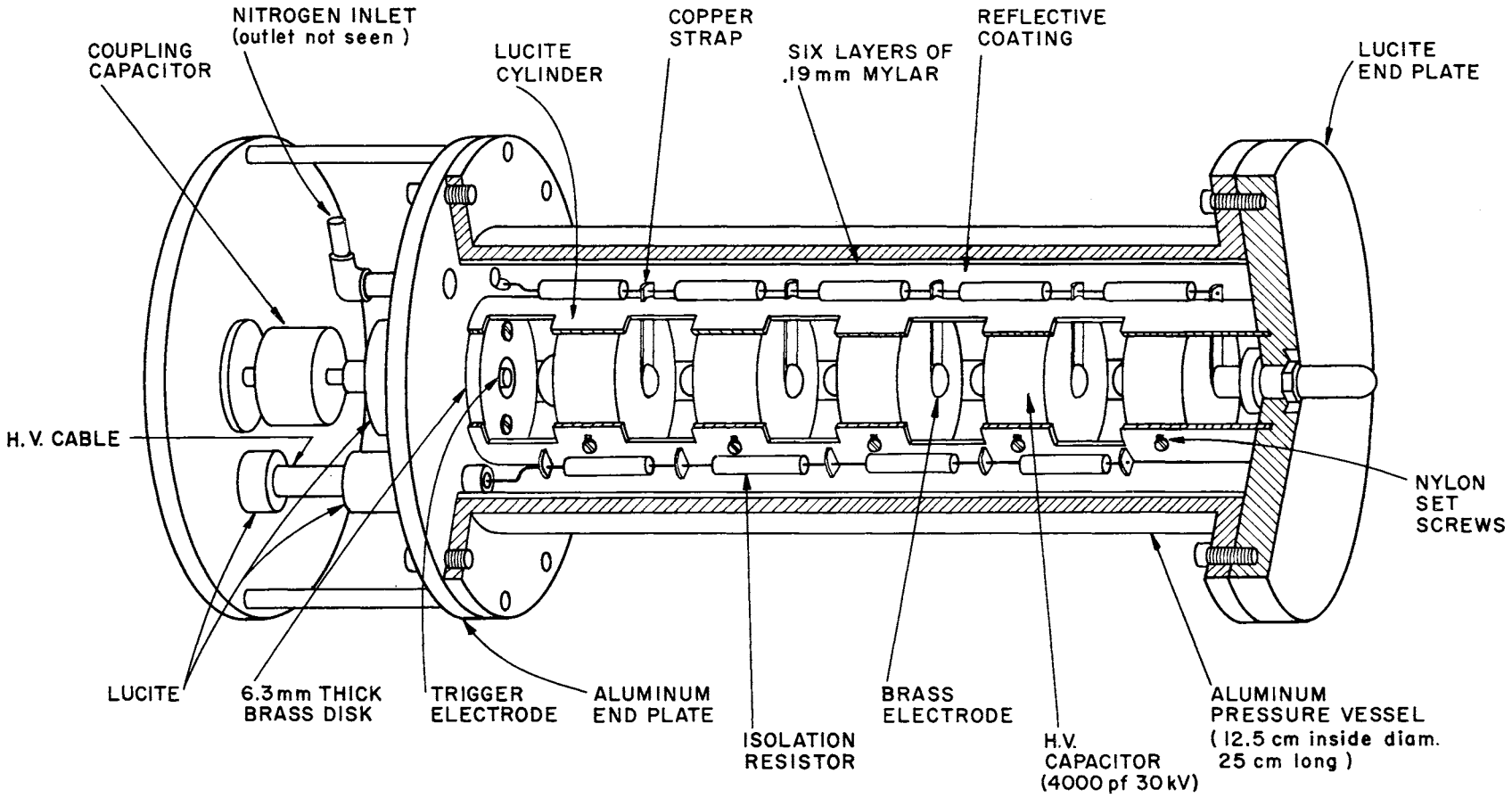

Figure 8. Mechanical Properties of the Marx Generator

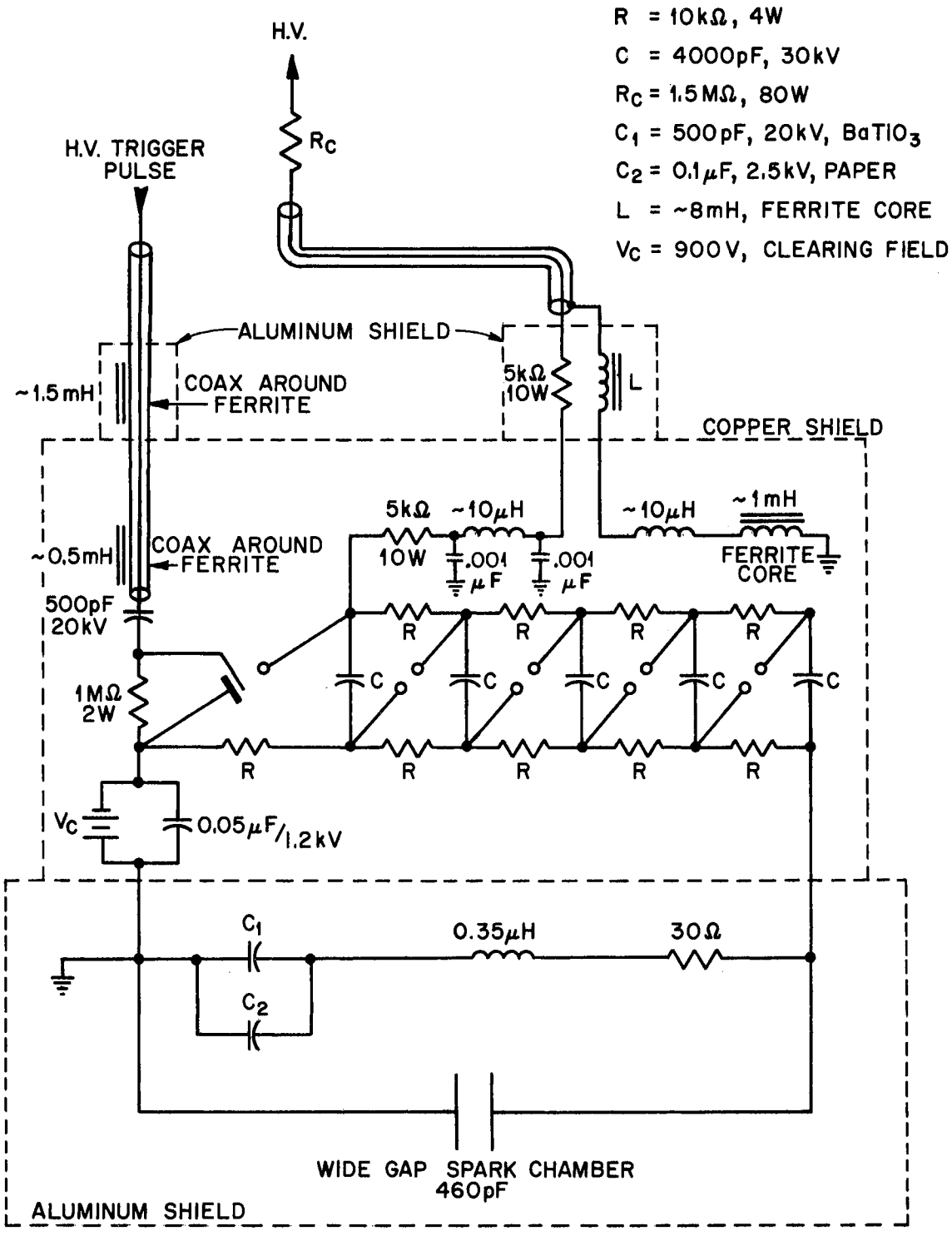

Figure 9. Marx Generator Electronics

A schematic diagram of the gas circulation and purification system is shown in Figure 10. Its purpose is to supply the wide gap spark chambers with gas which is free of water vapor, oxygen, and other contaminants. The gas composition was 88.2% neon, 9.8% helium, and 2.0% ethyl alcohol vapor at the entrance port to the chambers.

Circulation of the gas was accomplished with a mechanical vacuum pump which was modified so the exhaust was into the closed system. This pump was followed by an oil filter and then by a liquid nitrogen cold trap to remove alcohol vapor, water vapor, oxygen, nitrogen, and any organic vapors which may have outgassed into the system. The purified gas then flowed through a reservoir containing ethyl alcohol vapor in contact with liquid alcohol. The flow of gas was adjusted and calibrated to produce a 2% concentration of ethyl alcohol in the gas leaving the reservoir.

Due to leaks in the system the supply of gas had to be replenished occasionally. A diaphragm was used to monitor the pressure differential between atmosphere and the exit from the chambers. If this differential pressure fell below 0.0025% of an atmosphere an electric solenoid valve was opened to a reservoir and gas was admitted until the proper pressure differential was reestablished. A negative pressure bubbler was supplied to vent air into the system in the event of a

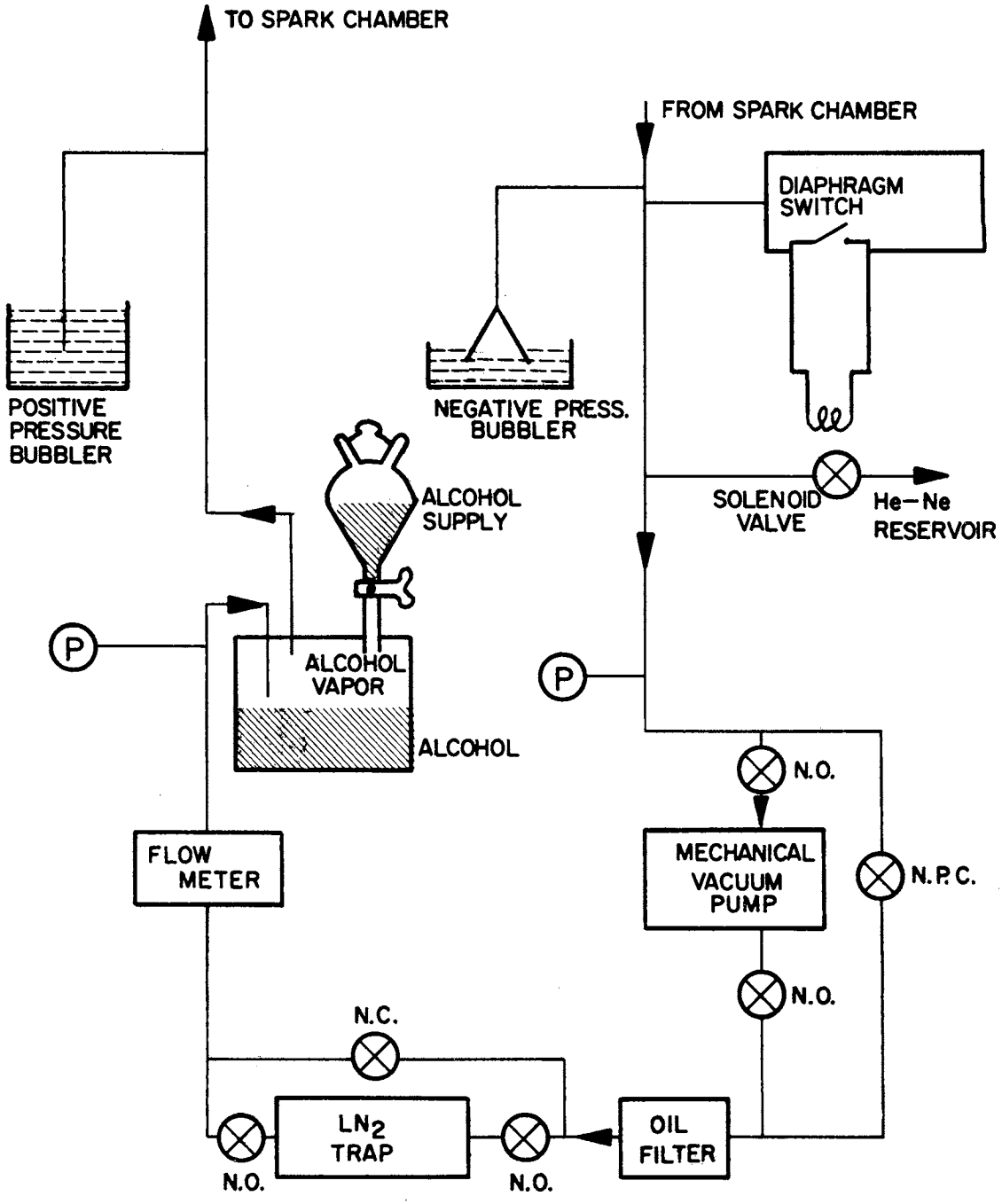

N.O. — NORMALLY OPEN
N.C " CLOSED
N.P.C. " PARTLY CLOSED

Figure 10. Spark Chamber Gas Purification and Circulating System

severe pressure differential which might cause the chambers to collapse. A positive pressure bubbler was also included to handle over pressures in the system by venting gas into the atmosphere if the system pressure exceeded atmospheric pressure by 0.025%.

The gas flow rate was one chamber volume every four hours. The flow was held constant enough to keep the ethyl alcohol concentration fixed to within ± 0.1%.

Optics and Photography

Figure 11 shows the optical system used to record four views of each event plus a frame number. There are two 90° stereo views of all 4 spark chamber gaps which are used for measuring an event, and two 30° stereo views of only the front 2 gaps used for resolving possible ambiguities in track identification. To position the views on the film, each view plus the frame number panel has its own adjustable mirror located just below the camera. Figure 12 shows a ray diagram of the mirror system. Near every corner of the spark chamber is at least one fiducial light which is pulsed for each event. The fiducials were 3 mm diameter machined plexiglas spheres connected to a 14 cm long plexiglas light pipe. The bulbs at the end of each light pipe were pulsed with a 45 volt pulse of 20 msec duration. The fiducial locations were surveyed relative to the beam survey line before and after the experiment and found to have the same positions within the accuracy of the survey ($\sim 75\mu$).

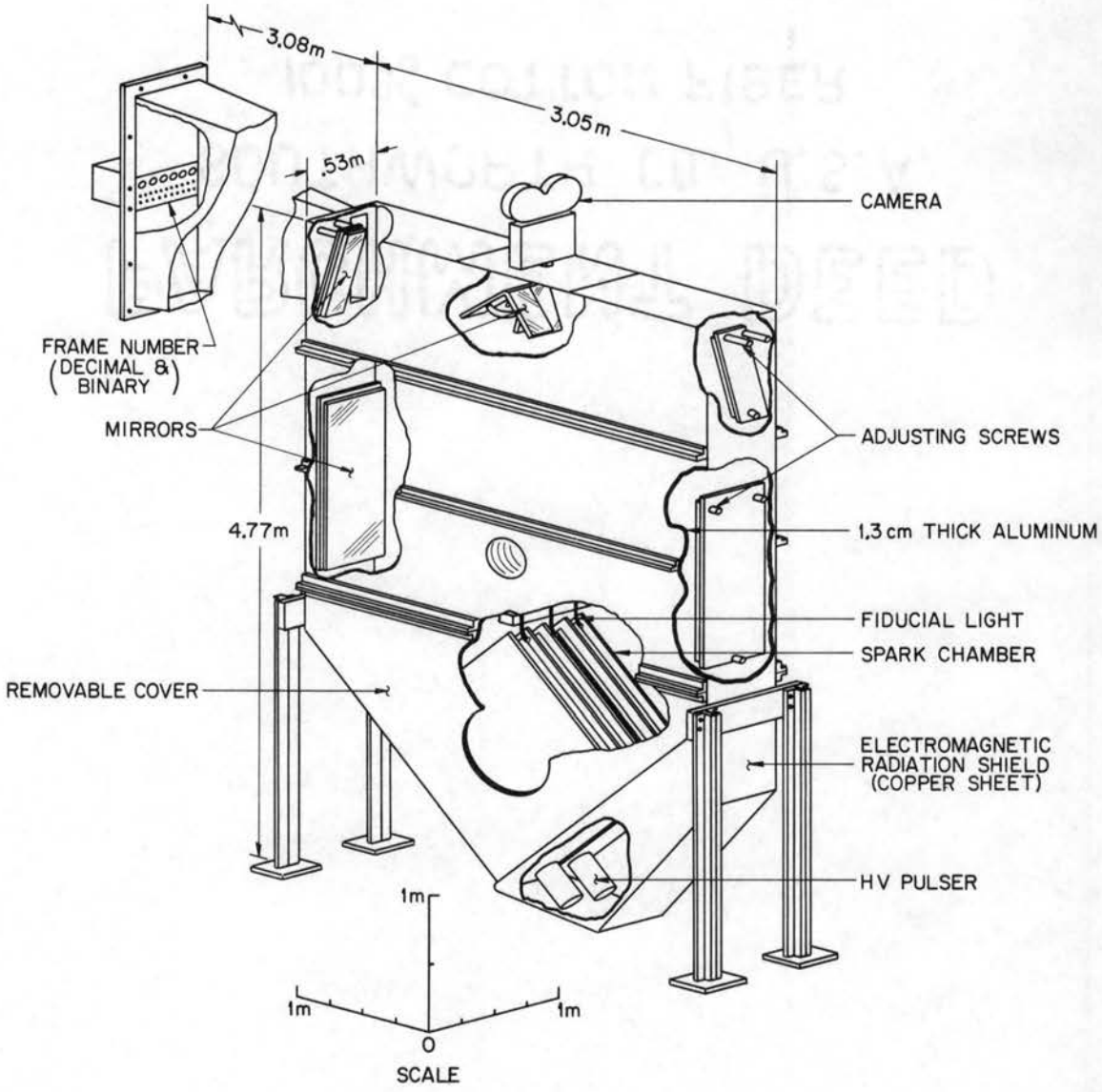

Figure 11. Optics System

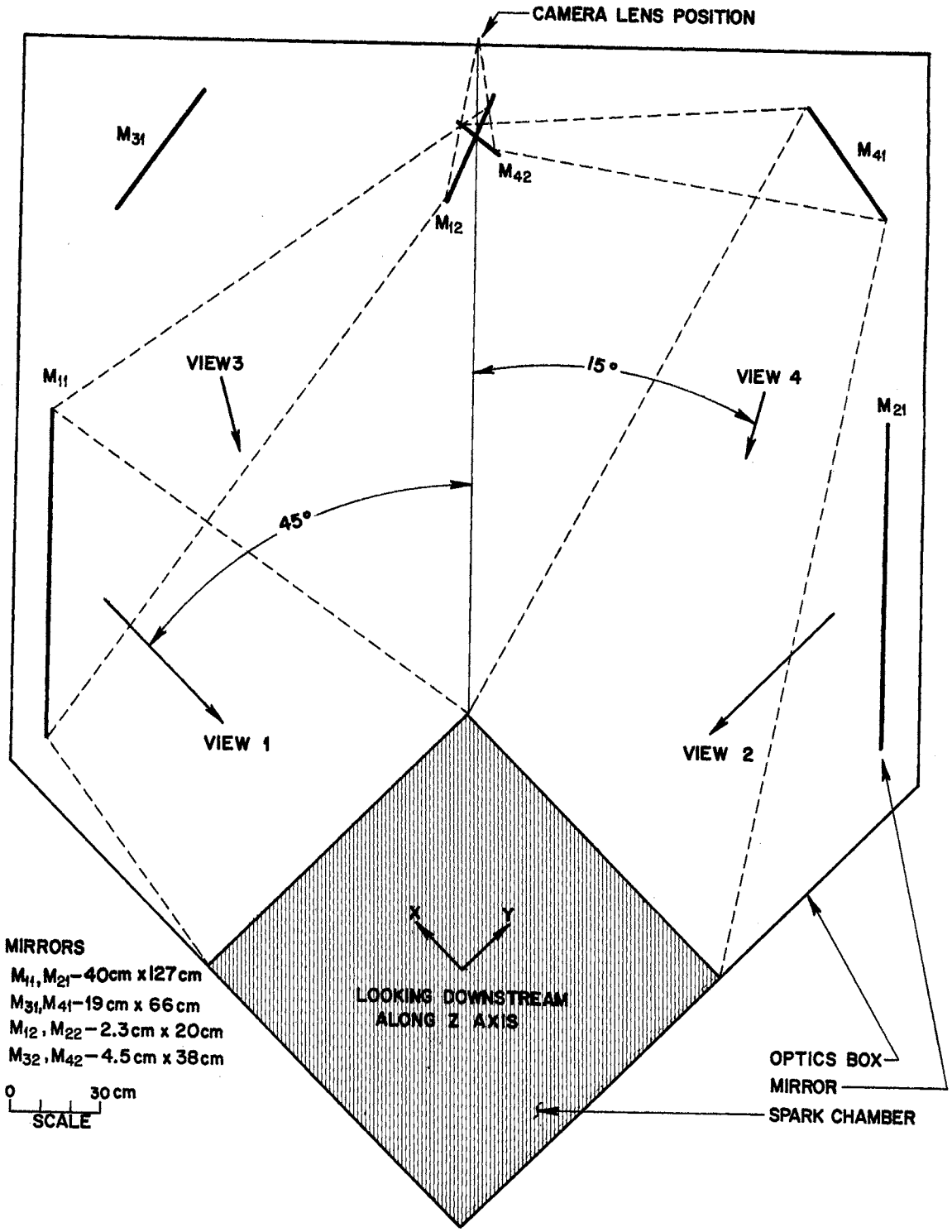

Figure 12. Ray Diagram of the Mirror System

A 35 mm double frame camera was used to record the wide gap chamber events (7). Since only one picture was taken each ZGS pulse, the fast advance capabilities of the camera were not utilized. The camera was fitted with an f/5.6 Schneider-Kreuznach Componon lens of 60 mm focal length which gave a film plane demagnification factor of 60. Pictures were taken at an aperture of f/5.6 on Eastman Tri-X film and developed by the ANL film processing group at 88° F for 3 minutes in D-19 developer. Figure 13 shows the film format.

Octant Scintillator Array

Figure 14 shows the octant scintillator counters labeled Q in Figure 3. Each of the eight 1.27 cm thick scintillators has a 71 cm radius and is epoxied to a plexiglas UVT light pipe which is in turn epoxied to a 56 AVP photomultiplier tube. Each of the eight counters is fastened separately near its tube to a steel I-beam octagon which has legs to hold it upright. The front layer of 4 counters is rotated approximately 45° with respect to the identical back layer. The electronic logic for these counters is described in the event logic section.

Stopping K^+ Counter

This section describes the design, construction, and performance of the K^+ detector. The counter had a geometrical acceptance for K^+ mesons with laboratory momenta between 250 and 600 MeV/c and

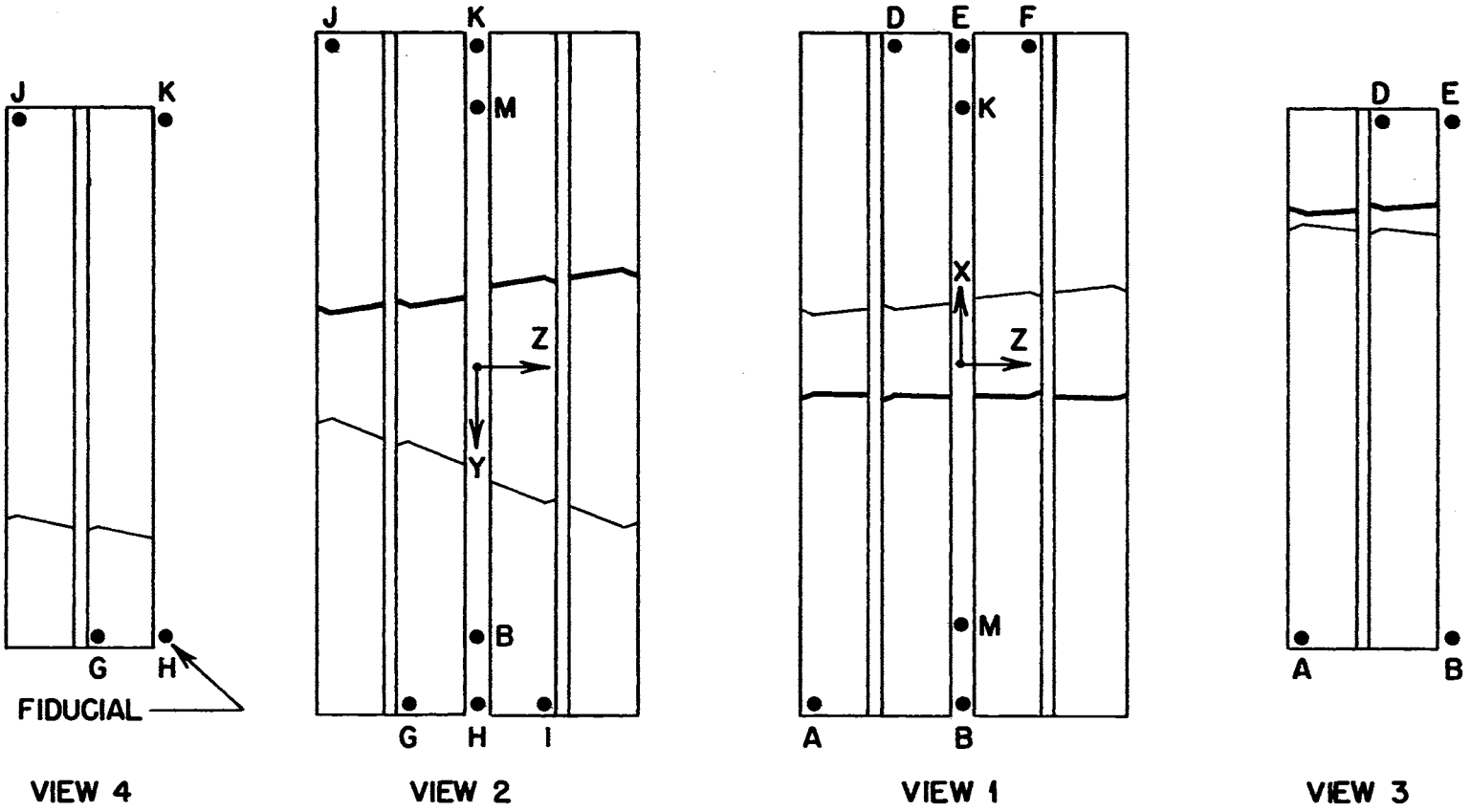

Figure 13. Film Format

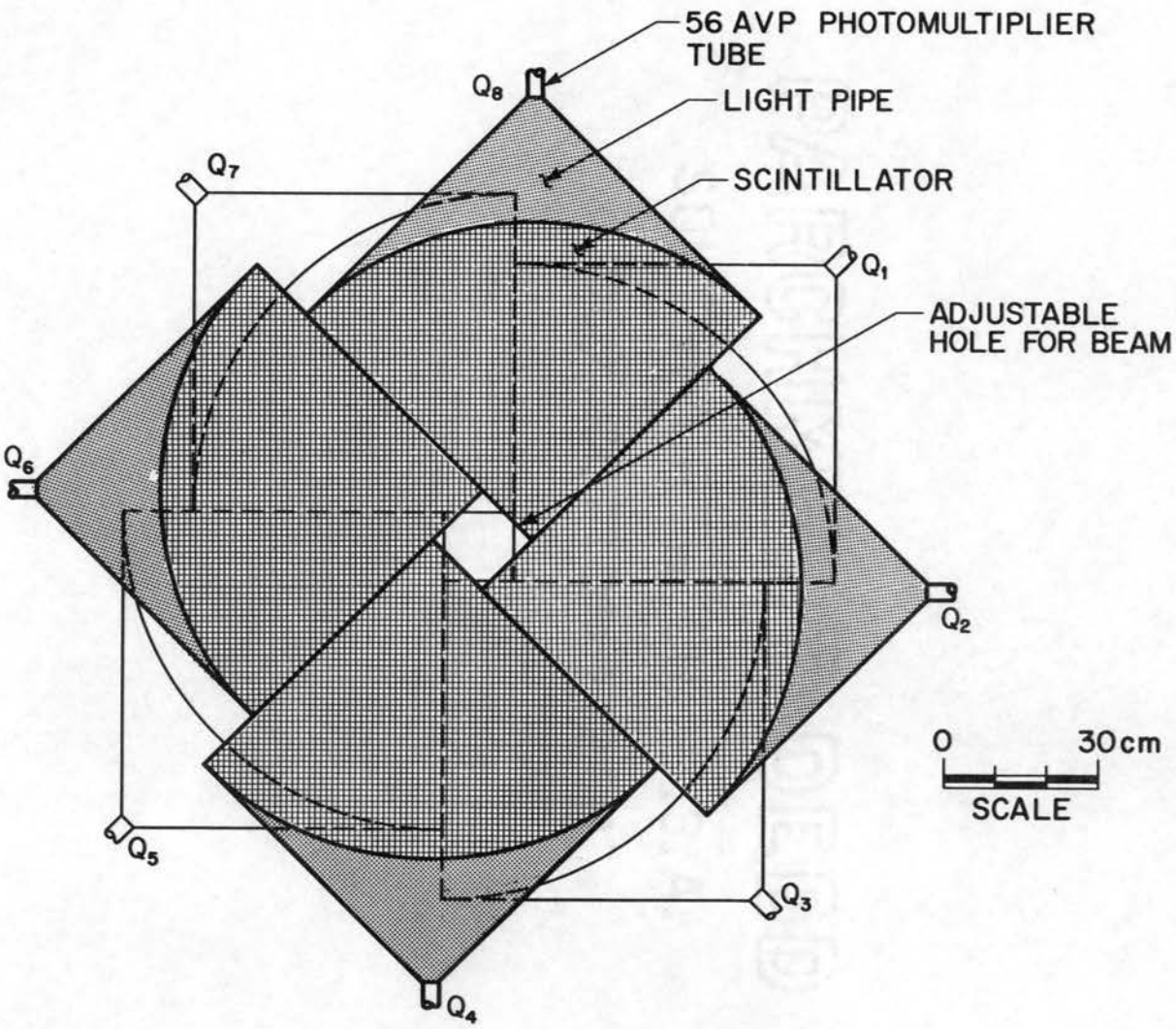

Figure 14. Octant Scintillator Array

and laboratory polar angles between 7^{o} and 35^{o}. For Σ^{+} production near threshold the K^{+} velocity is too small to get direct Čerenkov radiation; and because other charged particles are at least 100 times as numerous as K^{+}'s, a plastic scintillator is not desirable. The method is to build a counter which stops the K^{+} and detects the Čerenkov radiation from its highly relativistic decay modes. Because of the relatively short K^{+} lifetime, it is better not to stop the K^{+} in scintillation material since the pulse from the stopping K^{+} must be separate from the decay pulse. The size and shape of the K^{+} tank is determined by the range of K^{+} laboratory polar angles, the required distance from the hydrogen target to the counter (100 cm), and the requirement that charged decay products travel at least 10 cm in any direction inside the tank. Figure 15 shows the K^{+} tank and degrader in detail. The momentum vectors represent typical K^{+}'s from the center of the production target. The width of the K^{+} stopping region is due mainly to the size of the production target which allows a range of K^{+} polar angles to intersect a given radial point on the degrader. For the degrader, steel was chosen in preference to lead because of its better stopping power, availability, low cost, and relative ease of handling and supporting. One .63 cm thick steel plate has the equivalent stopping power of 4 cm of water.

The tank was filled with distilled water (Čerenkov threshold $\beta = .76$); so that the two body decays $K^{+} \rightarrow \mu^{+} + \nu$ ($\beta_{\mu^{+}} = .91$, branching

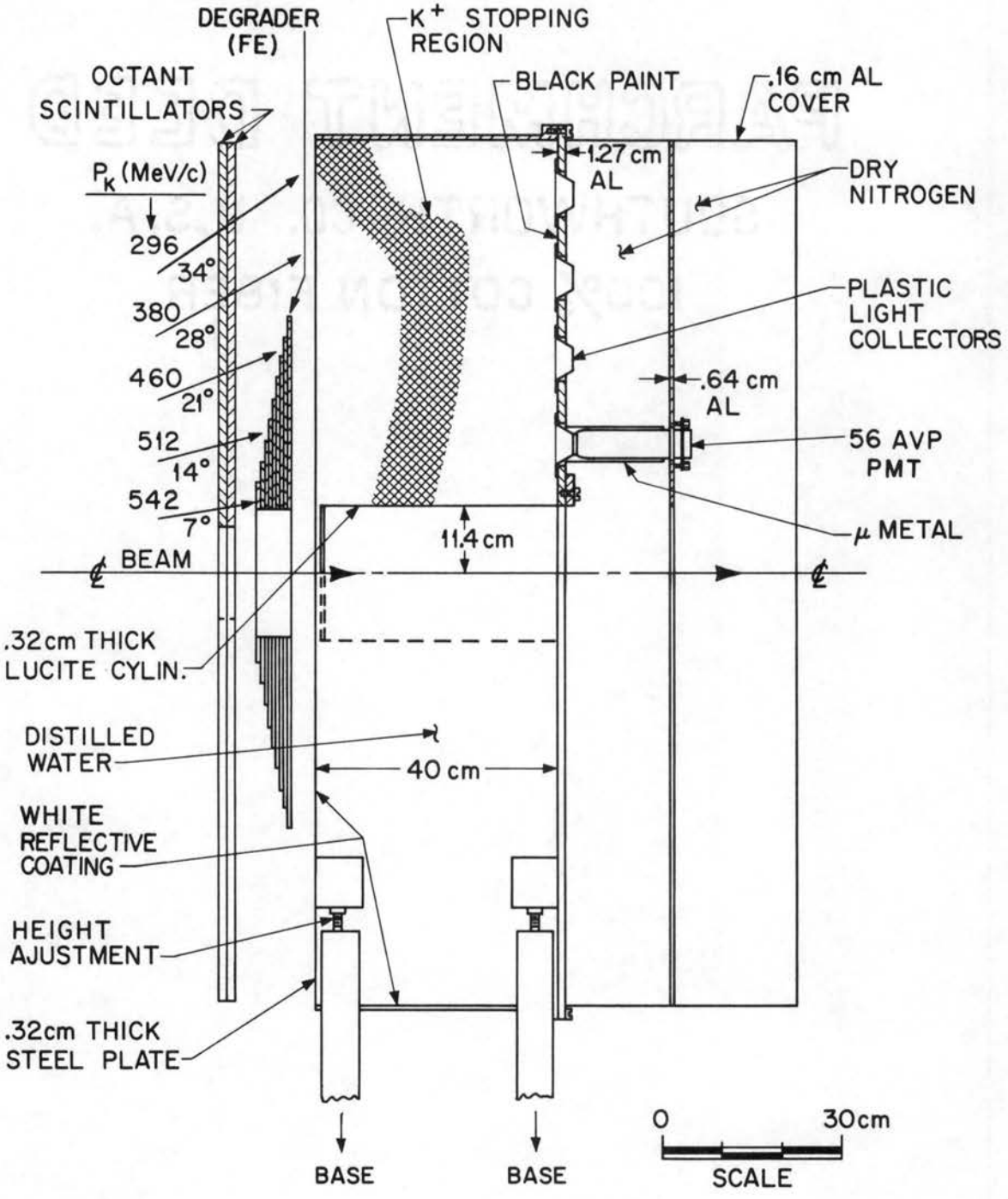

Figure 15. Stopping K^+ Counter

ratio = .63) and $K^+ \rightarrow \pi^+ + \pi^o$ (β_{π^+} = .82, branching ratio = .21) were accessible for detection. Seventy-two 56 AVP photomultiplier tubes were optically coupled to plastic reflectors (Lexan polycarbonate, n = 1.59) with silicon grease and held in a spring loaded mounting to insure stability. The light collectors were mounted through holes in the rear aluminum plate with RTV silicon rubber for sealing. Eight 1.5 mm diameter threaded stainless steel rods cross the inside of the tank to prevent bowing of the 3 mm front plate when the 6150 ℓ tank is filled. To reduce beam interactions and prevent random beam accidentals the water is excluded from the central region by a hollow plexiglas cylinder mounted through a hole in the rear plate. To detect light from charged particles which decay away from the tubes the front face and sides of the tank are coated with white magnesium oxide paint (8); the rear face is black to prevent light from reflecting back and forth across the tank and causing a slowly decaying output pulse.

Since the counter was required to have a high gain and the expected count rate was low, two high gain, low rate photomultiplier bases supplied 36 tubes each. Each base had a resistive voltage divider chain which dissipated 10 mA and operated at a negative high voltage. All 72 photomultipliers were tested in a light box with a standard source and chosen so that their gains did not differ by more than 30 %. The relative time delay of each tube pulse into a connector panel at the rear

of the counter was equalized using a barium-titnate light source whose trigger pulse also triggered a Tektronix 661 sampling oscilloscope. To narrow the output pulse the second output line of each anode had a 1.3 nsec 50 Ω clipping cable terminated with a 12 Ω short. The 72 outputs were added in 12 six channel linear passive resistive mixers which were in turn passively added to produce a single output pulse, so that any one tube has a 1/72 gain through the mixers. Two EG&G amplifiers, each with a gain of 4.4 and used in cascade, follow the mixers. Figure 16 shows the arrangement of the photomultiplier tubes on the rear plate of the tank. Table II gives some parameters of the counter.

The counter was tested with stopping K^+ mesons using a low momentum K^+ beam. Figure 17 shows the physical layout and electronic logic used for the stopping beam test. K^+ mesons were selected by time of flight measurement with counters separated by 7.2 meters, which for a 750 MeV/c beam corresponds to a time of flight difference of 5.0 nsec between kaons and pions. The width of the coincidence peak was 1.3 nsec. Figure 18 shows the coincidence curve between the Čerenkov counter and the beam counters with the degrader removed. Figure 19 shows the tail of the coincidence curve with the degrader in place and set to stop K's in the center of the water tank. Plotted on a log scale the counting rate in the tail should decrease with a slope equal to the reciprocal of the K^+ lifetime (12.35 nsec). Figure 20

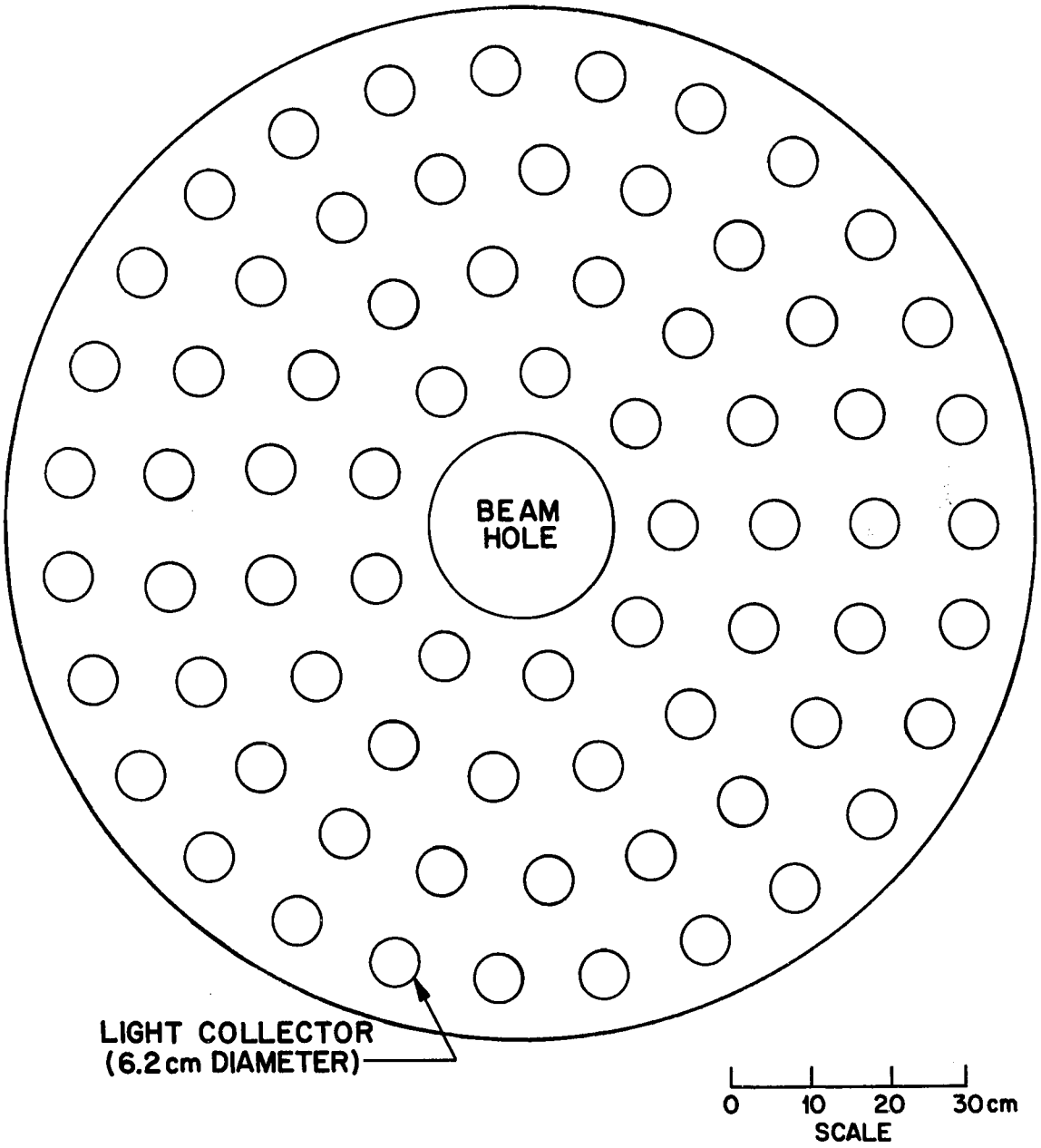

Figure 16. Photomultiplier Tube Arrangement on Rear Plate of the K^+ Tank

TABLE II

PARAMETERS OF THE STOPPING K^+ COUNTER

Volume	6150 liters
Total Mass	6400 kg
Steel Degrader Mass	90 kg
Total Inside Area	4.93×10^4 cm^2
Area of Light Collectors	2.18×10^3 cm^2
Radiator	Distilled water, n = 1.33
Mean Free Path of Visible Photons in Radiator	20 m
Photons/cm for S_{11} Response from $\beta = 1$ Particles	208
Minimum β Detected	0.76
Initial β of μ^+ from $K^+ \rightarrow \mu^+ \nu$	0.91
Initial β of π^+ from $K^+ \rightarrow \pi^+ \pi^o$	0.82

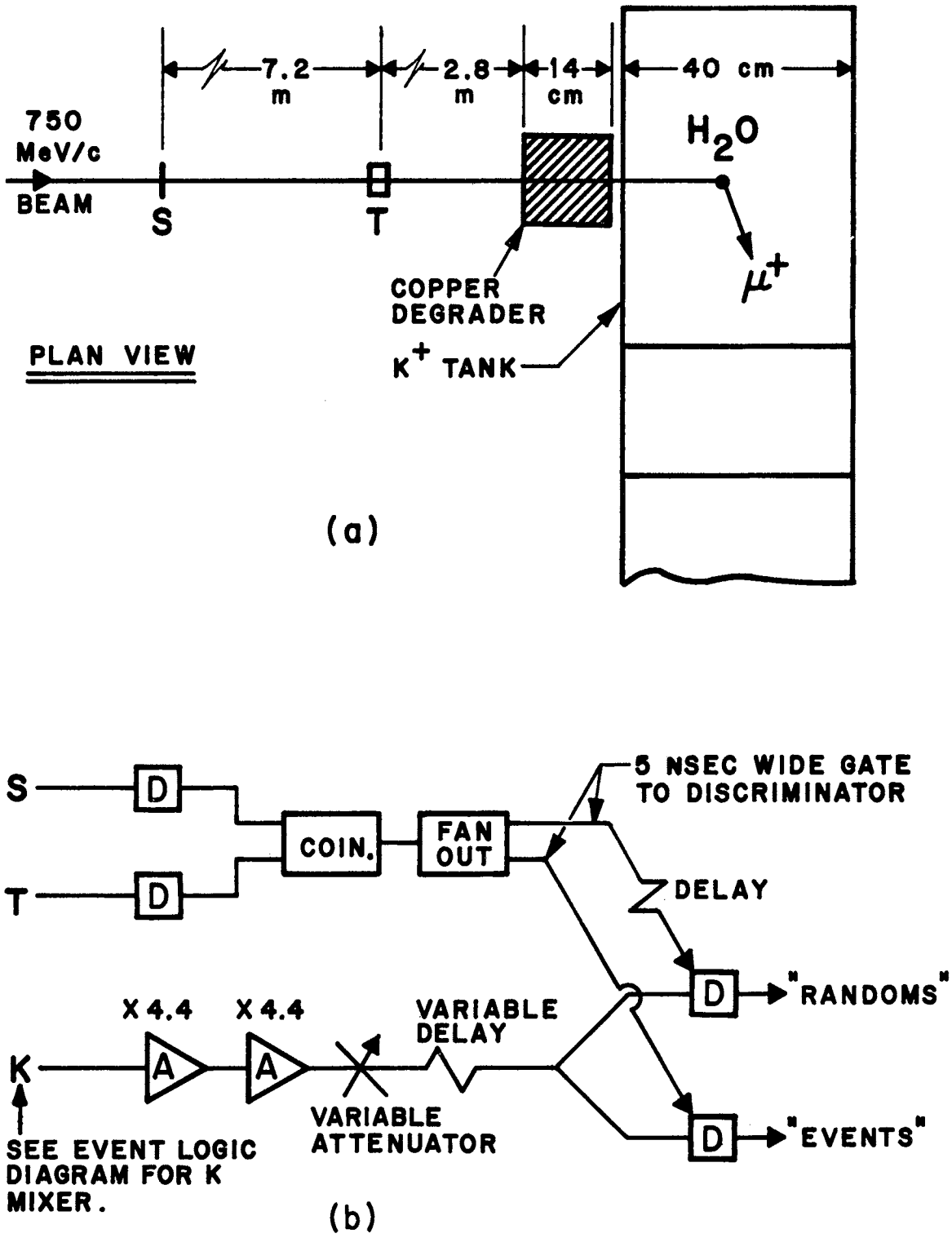

Figure 17. a) Physical Setup and b) Electronic Logic for the Stopping K^+ Beam Test of the K^+ Counter

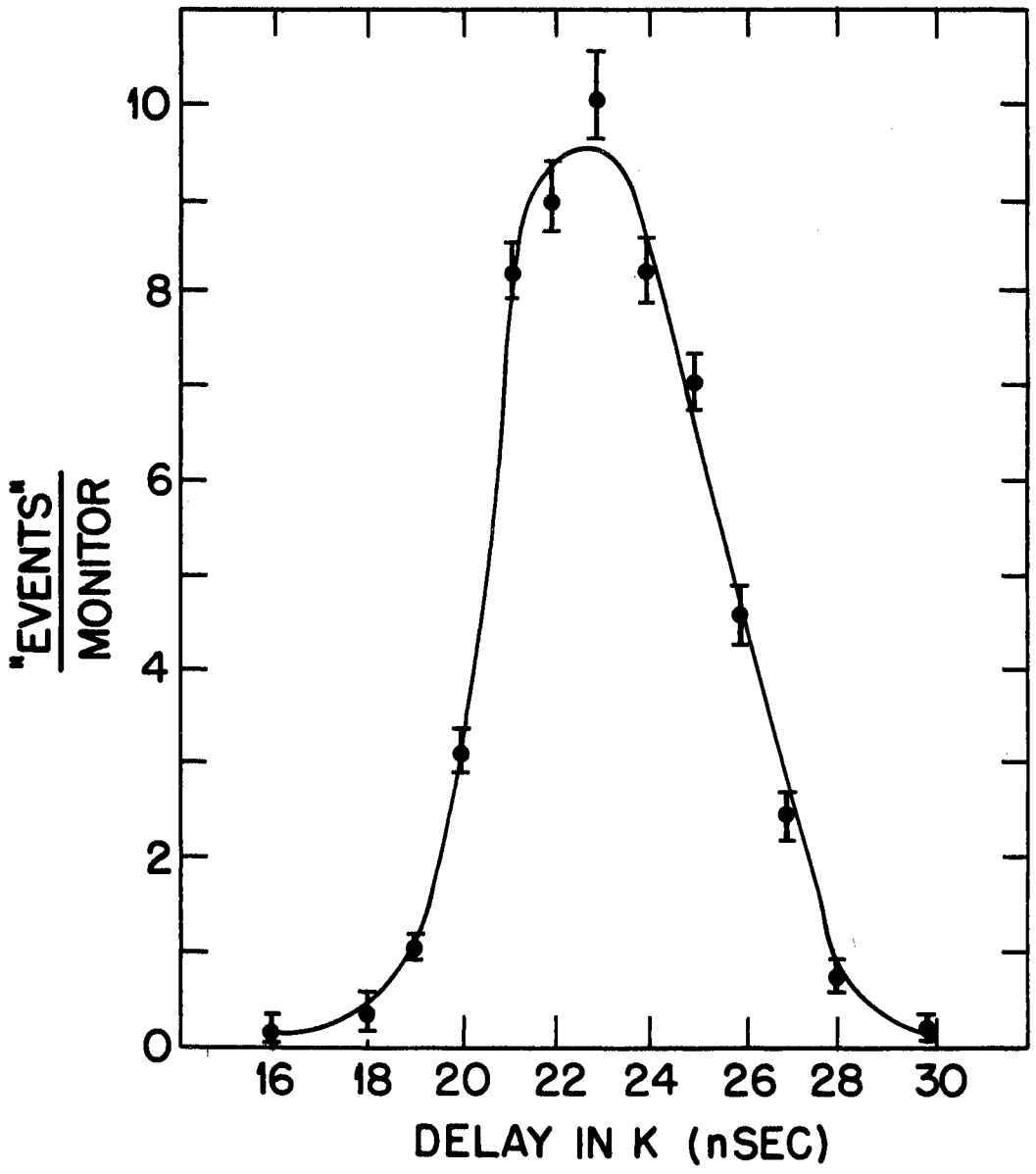

Figure 18. Event Rate Versus K Delay for $\beta = .83$ Particles Through the K^+ Counter

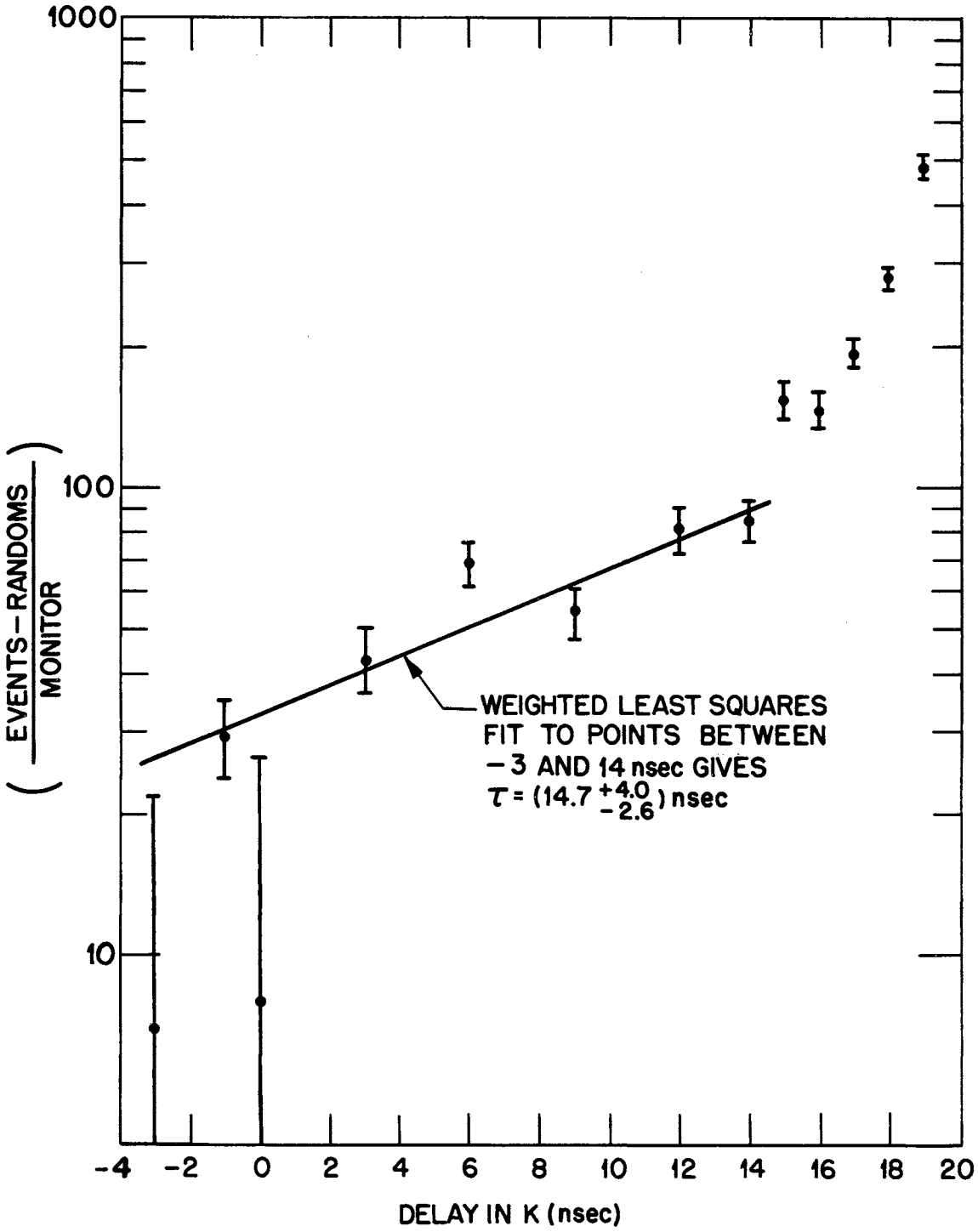

Figure 19. K^+ Counter Coincidence Curve for K^+ Mesons Stopping in the Counter

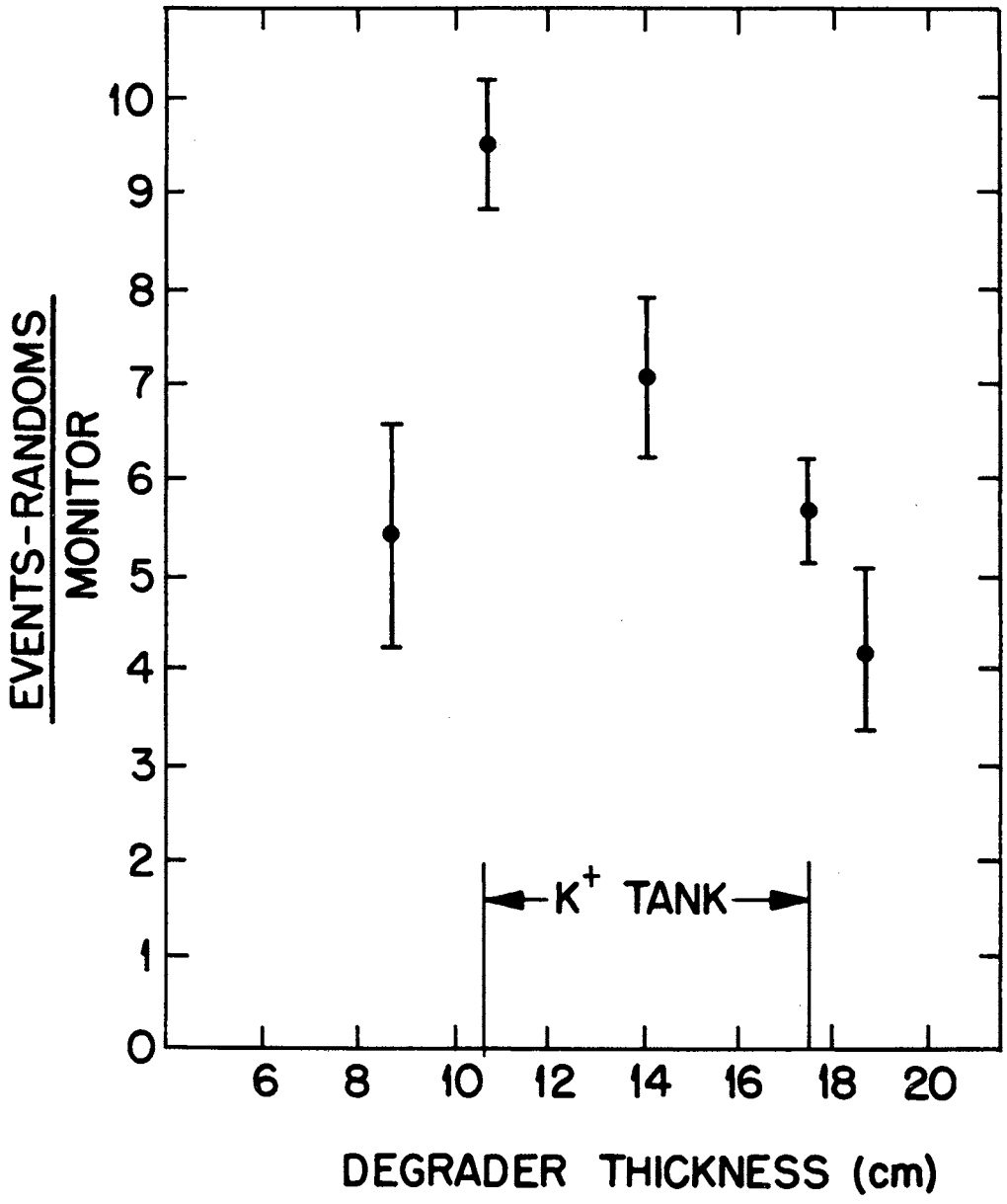

Figure 20. Stopping K^+ Signal Versus Degrader Thickness

shows the stopping K^+ signal versus degrader thickness. The efficiency of the counter for detecting stopped K^+ mesons was estimated by measuring the ratio (event rate/beam rate) and applying the following correction:

1) randoms in the event rate

2) randoms in the beam rate

3) beam decay loss from last beam counter to K^+ counter

4) beam interaction loss in degrader and water

5) stopped K^+ decays occurring before K^+ gate opens

6) stopped K^+ decays occurring after K^+ gate closes

Figure 21 shows the dependence of the estimated efficiency on the attenuation in the K^+ signal.

Event Logic

Figure 22 shows a diagram of the electronic logic used to record an event. Counters P and A selected beam particles entering the hydrogen target. The eight counters Q_i were required to select two and only two charged particles associated with a beam particle. To accomplish this the logic was arranged to register a Q output when any two of the eight 45° sectors (octants) had simultaneous pulses. The eight octant coincidence outputs were mixed in a linear adder whose output pulse height was linearly proportional to the number of simultaneous input pulses. The threshold and window widths of the

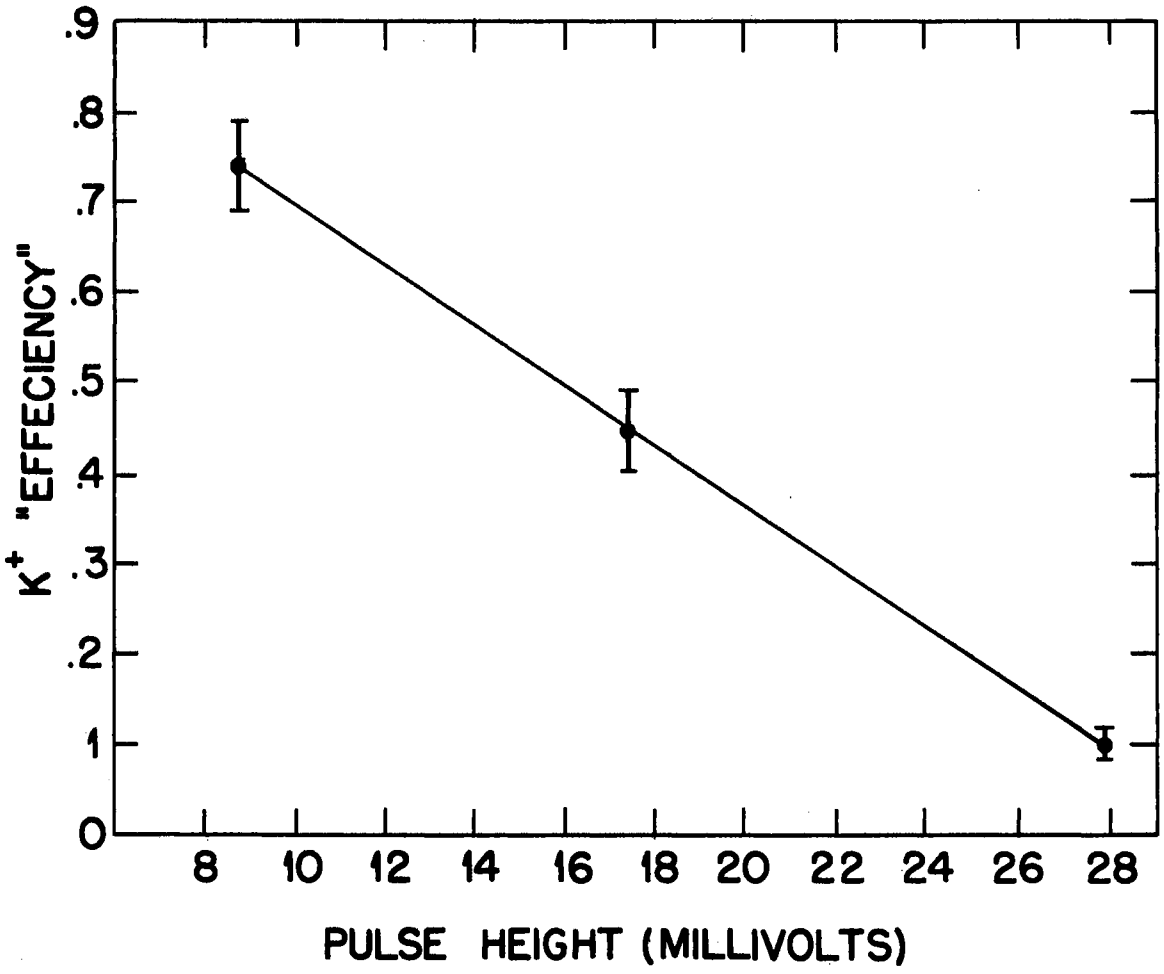

Figure 21. Estimated Efficiency (see text) Versus Minimum Pulse Height from Passive K Mixer Needed to Register an "Event". Errors are Statistical Only.

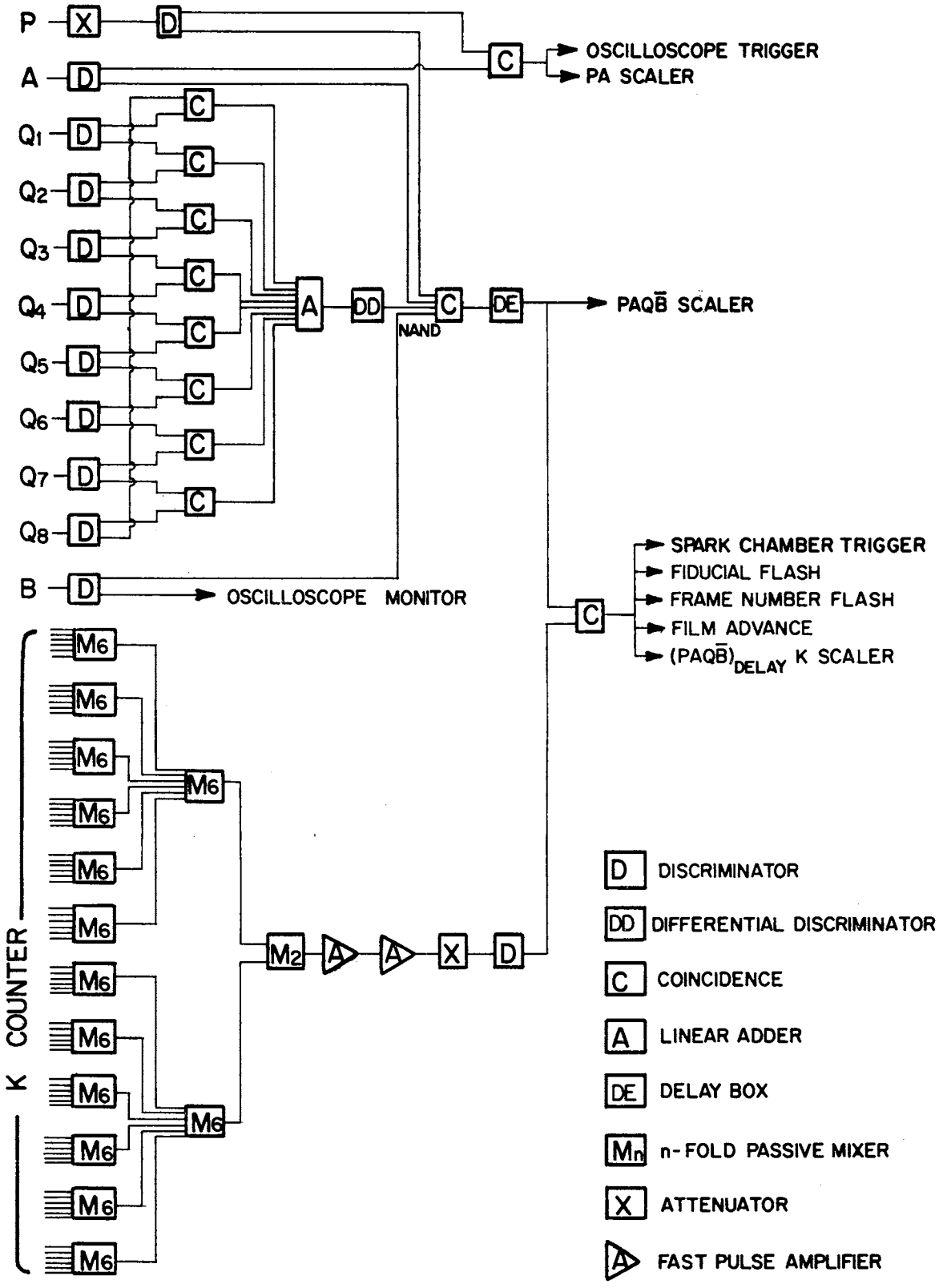

Figure 22. Electronic Logic Diagram

differential discriminator were adjusted so that the discriminator triggered when there were two and only two simultaneous pulses into the linear adder. The output of the differential discriminator was then put in coincidence with P and A and in anticoincidence with a downstream beam counter B (Figure 3). The resultant $PAQ\overline{B}$ output was fed into a dual concidence circuit and timed to a delayed pulse from the stopping K^+ counter. Since fast pions will also count in the K^+ counter, the signal $PAQ\overline{B}$ was delayed six nsec with respect to the time that a fast pion would reach the K^+ counter. Figure 23 shows the coincidence curve between the K^+ counter and $PAQ\overline{B}$. When an event was registered by the logic, high voltage pulses were applied to the wide gap and beam spark chambers, the fiducial and frame number lights were flashed, and the film was advanced. The time delay between the occurrence of the desired reaction in the hydrogen target and the application of the high voltage pulse to the wide gap chambers was 310 nsec.

Data Acquisition

The data was accumulated at pion momenta 1106, 1134, and 1164 MeV/c during a period of approximately 7 days. The following drift checks were made about once every two hours.

1) beam magnet settings

2) all phototube voltages

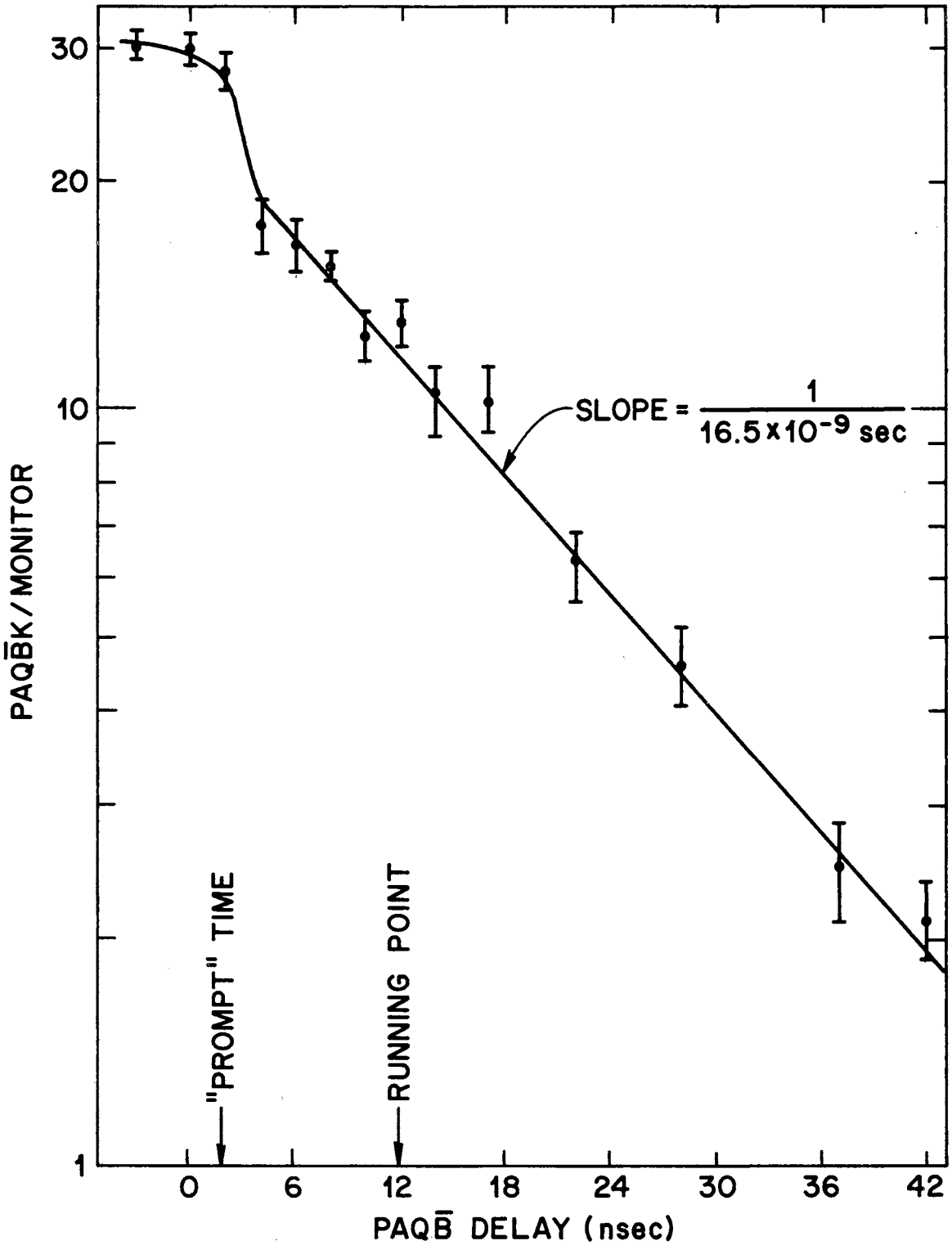

Figure 23. Coincidence Curve Between the K^+ Counter and PAQ$\overline{B}$

3) logic voltages

4) liquid hydrogen level in target

5) Marx generator nitrogen pressure and high voltage

6) delay of high voltage pulse to wide gap spark chamber

7) pion counter gain (see section describing beam counters).

Other checks made at least once every eight hours were:

1) clearing field on wide gap chamber

2) test strips from wide gap and beam chamber cameras

3) response of Q counters to a Co^{60} source

4) pressure in beam helium bags.

Finally, as a delayed check on the beam divergence and position and on the relative position of the beam chamber to the wide gap fiducial system, both chambers were simultaneously triggered (PAB) on beam tracks about once a day.

CHAPTER III

DATA ANALYSIS

Scanning and Measuring

All pictures were scanned once for events consisting of two unscattered tracks projecting into the region of the hydrogen target. One track was required to pass through a fiducial volume which was larger than the target by 1 mm on the scanning table, where the projected image was 1/3 of true size. The other track was required to come from a cone shaped region (Figure 24) which was sufficiently large to safely include all possible sigma decay configurations.

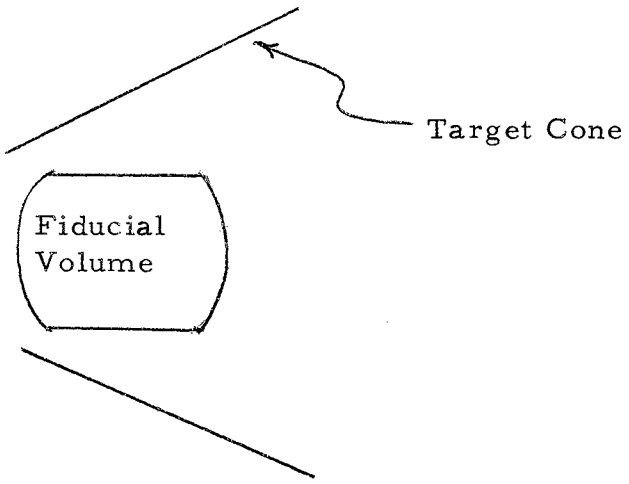

Figure 24. Fiducial Volume and Target Cone Used in Scanning

Both of these tracks were required to pass through the Q counters. An unscattered track was defined as one which scattered less than 1^{o} in the spark chambers. If more than two tracks were acceptable, the event was rejected. Tracks which resulted in two or more prong interactions in any plate of the spark chamber were also rejected. Table III gives the results of a scanning test to determine the type of events which triggered the logic.

TABLE III

SCANNING TEST SUMMARY

Total Scanned	189 frames
Labeled for Measurement	35 (18.5 ± 3) %
Rejected	154
Reasons for Rejection:	
a) Two or more tracks in Q but target requirement not satisfied.	54
b) Two tracks from target in Q but one or both have multiple coulomb scatter $> 1^{o}$.	17
c) One track in Q.	42
d) One track in Q plus beam tracks.	16
e) Beam track + backscatter.	10
f) Beam tracks only.	11
g) Three tracks from target in Q.	4

The selected events were measured on Hermes film plane digitizers which produced a paper tape containing the digitized coordinates of fiducials and sparks. The image viewed by the measurer was about one-half of true size. A reticle consisting of a dot centered in a circle was used in one measuring machine and a cross centered on a dot was used in the other machine. No difference in setting precision was observed for the two reticles.

For views 1 and 2 (Figure 13) the measurer set the reticle on seven fiducials in a prescribed order and digitized them by activating a RECOMP (9) computer to read the Hermes coordinates. The setting reproducibility on the fiducial coordinates was approximately $\pm 2\ \mu$ on the film plane, which corresponds to ± 0.12 mm in real space. Forty to fifty points were measured on each track: either ten to twelve measurements on each of the four sparks or twenty to twenty-four points on each of the first two sparks. The latter method was used in an attempt to reduce the effect of multiple coulomb scattering in the chamber plates and gas.

Experienced measurers could average seven events/hour during four hour shifts.

Event Reconstruction

The measured events were reconstructed in space using a CDC 3600 computer and a program called MAP (10). For input MAP needs:

1) Fiducial coordinates in real space.

2) Location and orientation of the camera lens.

3) Fiducial and spark point coordinates on the film plane (these data are on a magnetic tape which is copied from the measuring machine paper tape using a CDC 160-A computer).

The camera lens location and orientation were determined using program FINDCAMERA (11), whose input is the real space and film plane coordinates of at least five fiducials. When MAP has determined the best straight line fits to the two measured tracks, it calls subroutine EVENT which uses kinematics to reconstruct the event in space. It is assumed that the beam track's average direction and momentum are known (Figure 2), but not its spacial location. (For a given event this assumption results in approximately a ±4% uncertainty in the Σ^+ decay time, but when averaged over many events this uncertainty is negligible.) EVENT takes the first measured track to be the K^+ and with the assumed beam track can determine the production plane and Σ^+ production angle. The Σ^+ decay point is then determined by the intersection of the decay track and the production plane; and from the known sigma production angle, the production vertex is located. The procedure just described may result in a sigma produced backwards in the laboratory (kinematically impossible), in which case the fit is repeated with the second measured track as the K^+. The fit is not overconstrained, so that every properly measured picture fits a $\Sigma^+ \rightarrow p\,\pi^o$ or $n\,\pi^+$ hypothesis except for a small sample (< 1%) in which both measured tracks do not satisfy

the K^+ kinematic requirements. Figure 25 shows the laboratory geometry of a typical sigma event. The MAP output is a magnetic

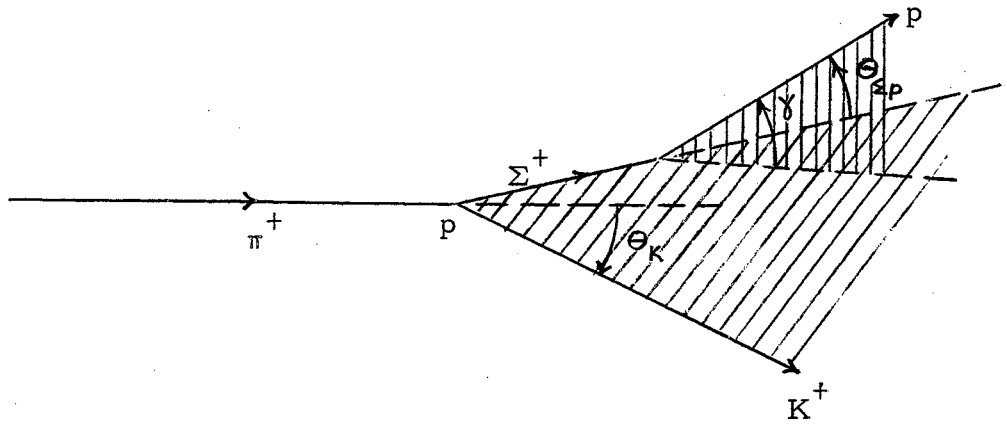

Figure 25. Laboratory Geometry of a $\Sigma^+ \rightarrow p + \pi^o$ Event (π^o Not Seen)

tape containing all geometry and kinematic information for the event.

Ionization Measurement

Since nearly all reconstructed events fit a sigma hypothesis, an additional means of selection is necessary. Also, in order to distinguish between the proton and charged pion decay modes and to resolve an ambiguity in the proton laboratory momentum, an attempt was made to measure the particles' ionization using the appearance of the wide gap tracks on the film(12).

Photometric measurements of the blackening of the film by the spark image were made with the device shown in Figure 26(a). The spark image was focused on the diffuse surface of the plexiglas light pipe. The voltage induced across the 500 kΩ resistor in Figure 26(b) is proportional to the current from the RCA 929 photocell and therefore proportional to the integral of the light flux striking the photocathode. The connectors to the photocell were potted in RTV silicon rubber to reduce leakage currents. In Figure 26(c) the squares represent two light pipe positions; one to measure the light transmitted by the film background, I_o, and the other to measure the light transmitted around and through the track, I. For each track the quantity $W = \frac{I_o - I}{I_o}$ was measured and averaged over at least two gaps. In attempting to identify sigma events with this method only the ratio of W's for each event was used since the brightness of any given track is dependent on the number and ionizing power of other tracks in the chamber. Corrections must be made for the variation of track brightness with track angle (5) and for nonlinearity of the film response. These two correction curves are shown in Figure 27.

To determine the resolution of the ionization measurement and check the angle and film correction curves, sigma events were selected using the beam track position given by the beam chamber. Figure 28 shows the deviations of beam tracks in the narrow gap chamber when matched to vertices of copunctual events measured in the wide gap system. The rms uncertainty is approximately 0.2 cm. Events which

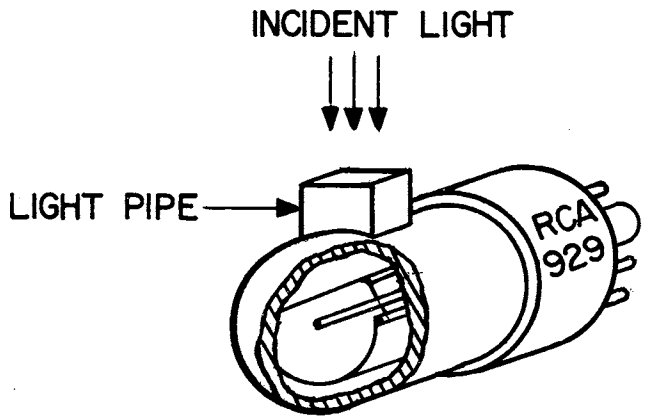

(a) MEASURING DEVICE

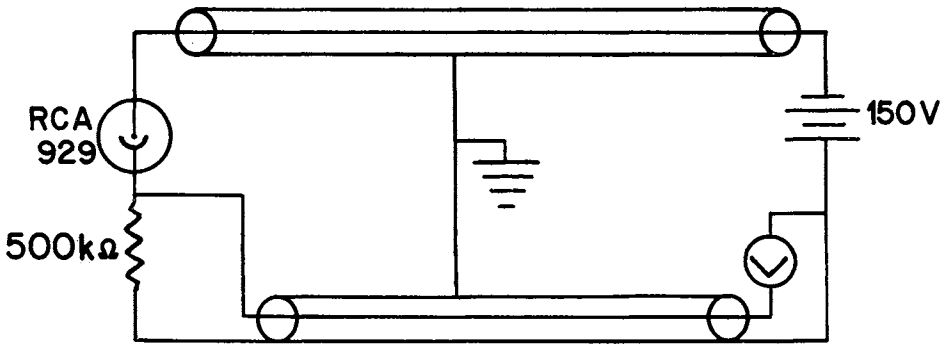

(b) CIRCUIT

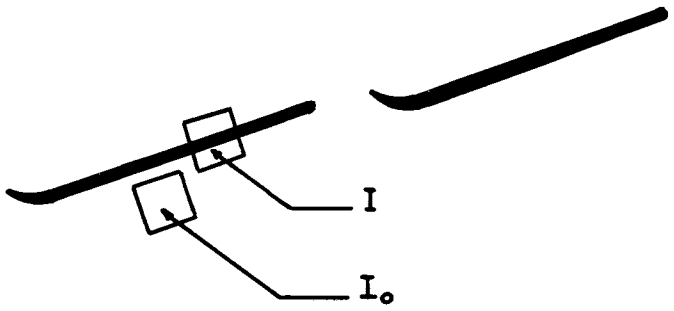

(c) POSITIONS MEASURED

Figure 26. Arrangement for Photometric Measurements of Wide Gap Tracks

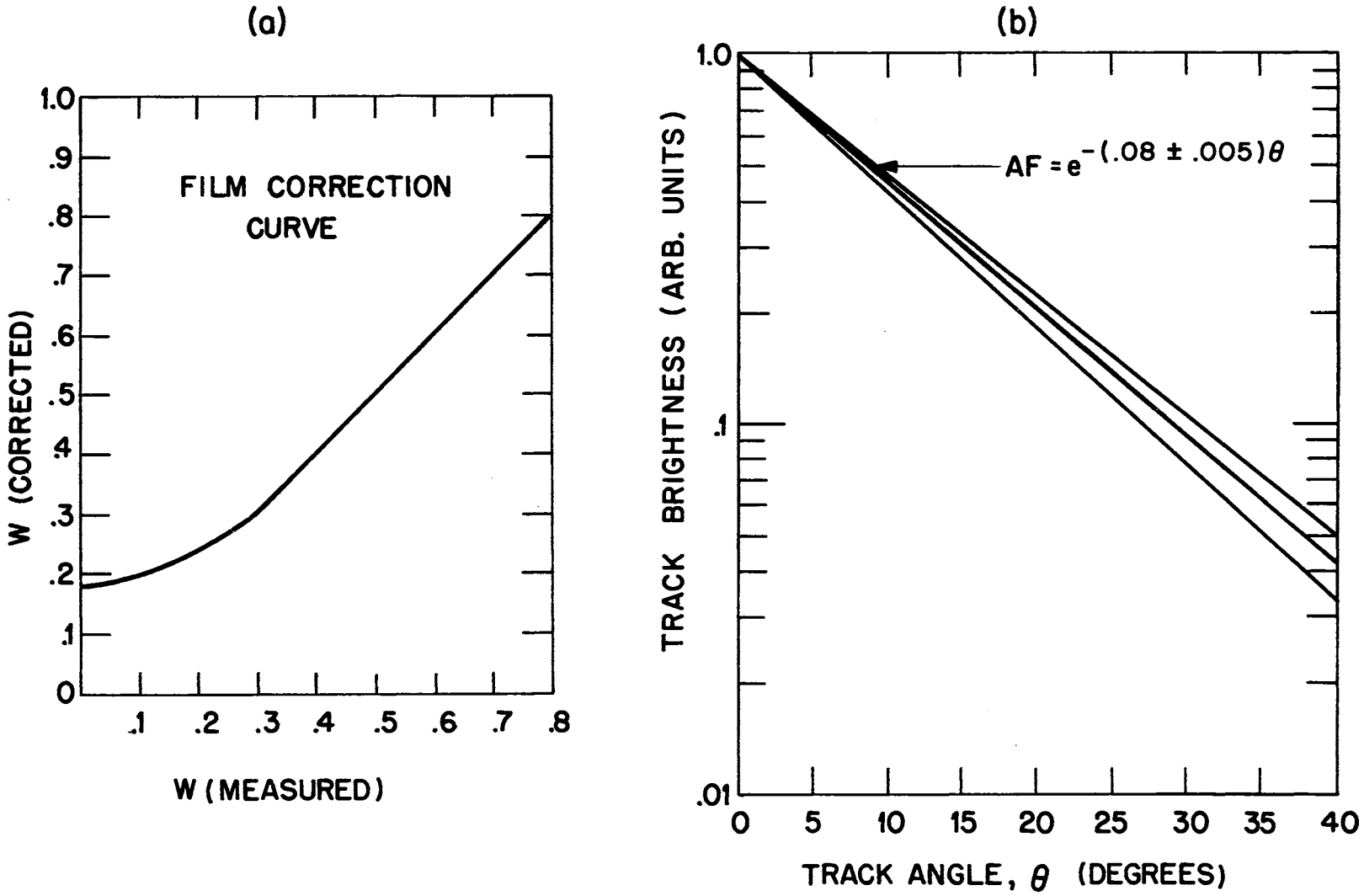

Figure 27. a) Film Correction Curve and b) Wide Gap Track Brightness Versus Track Angle

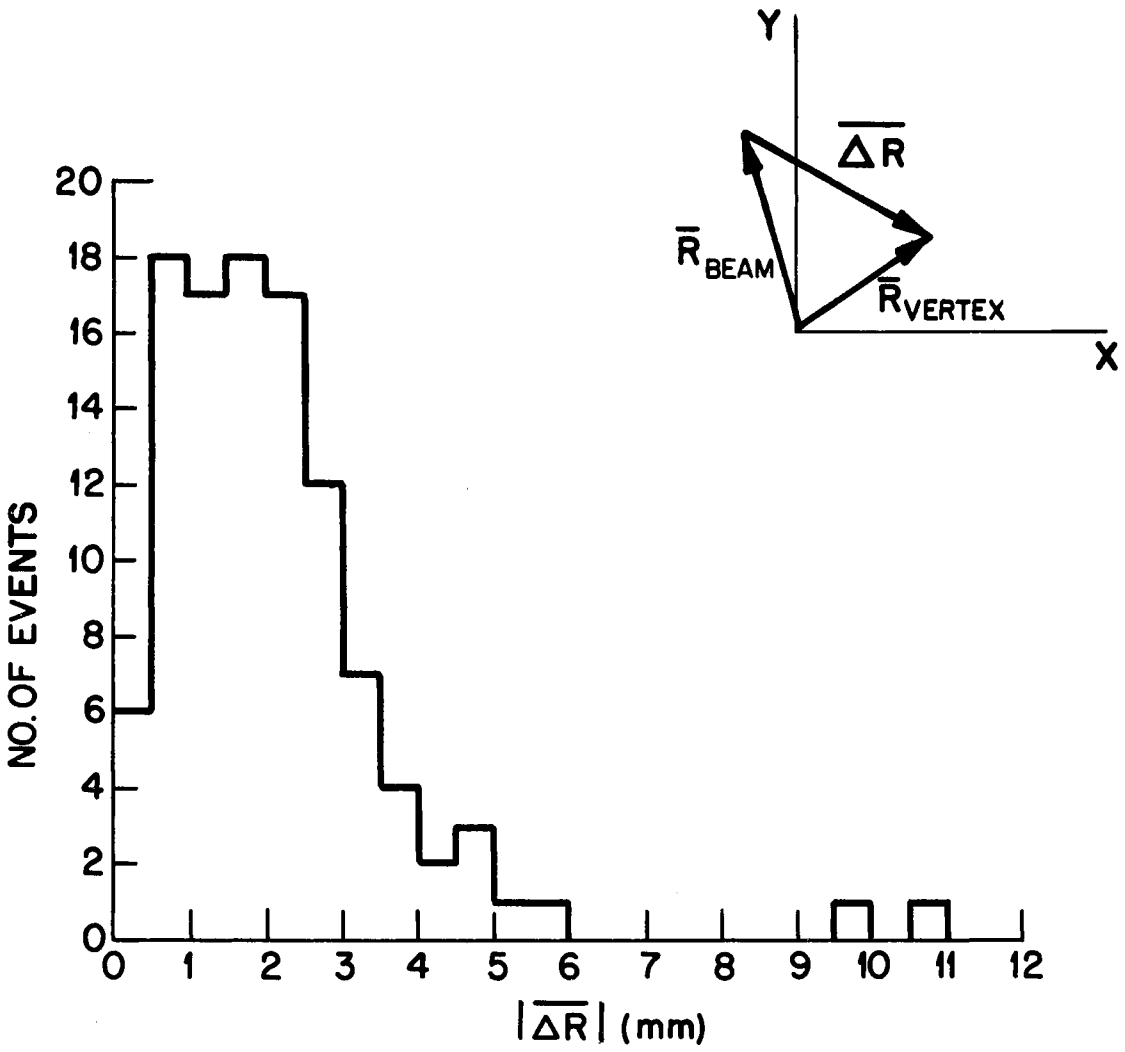

Figure 28. Beam Tracks Matched to Copunctual Vertices

had a sigma decay time greater than 0.8×10^{-10} sec, a coplanarity angle ($|\gamma|$ in Figure 25) greater than 0.05 rad, and a beam track matching the sigma production point better than three standard deviations (0.6 cm) and rejecting a copunctual hypothesis by more than three standard deviations were selected. The fractional deviations of the measured ionization ratio from the expected ionization ratio

$$\delta_i = \frac{(\text{measured ratio}) - (\text{expected ratio})_i}{(\text{expected ratio})_i} ,$$

or

$$\delta_i = \frac{M - E_i}{E_i} = \frac{M}{E_i} - 1 = \frac{\dfrac{W_{K^+}}{W_{\text{decay}}}}{\dfrac{(dE/dx)_{K^+}}{(dE/dx)_{\text{decay}}}} - 1 ,$$

with

$$i \equiv \text{pion, proton 1, or proton 2,}$$

were computed for the decay pion and both possible decay proton momenta. Figure 29 shows a plot of the smallest δ_i for each selected event. The solid curve is a least squares fitted gaussian centered on $\delta = 0$.

Figure 30 is a spark chamber photograph of a sigma event selected by the criteria described above. The light track is the K^+ which is 1.6 times minimum ionizing with a space angle of 16°. The heavier track is the decay proton which is 4.5 times minimum ionizing with a space angle of 20°.

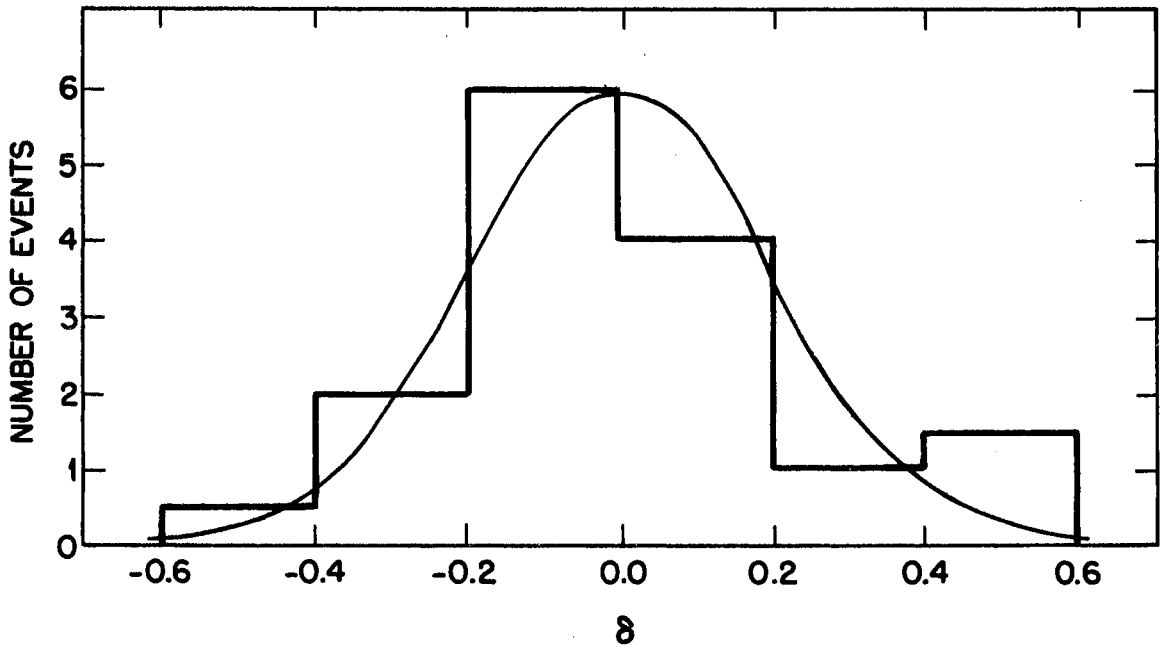

Figure 29. Fractional Deviation, δ, of the Measured Ionization Ratio from the Expected Ionization Ratio for Sigmas

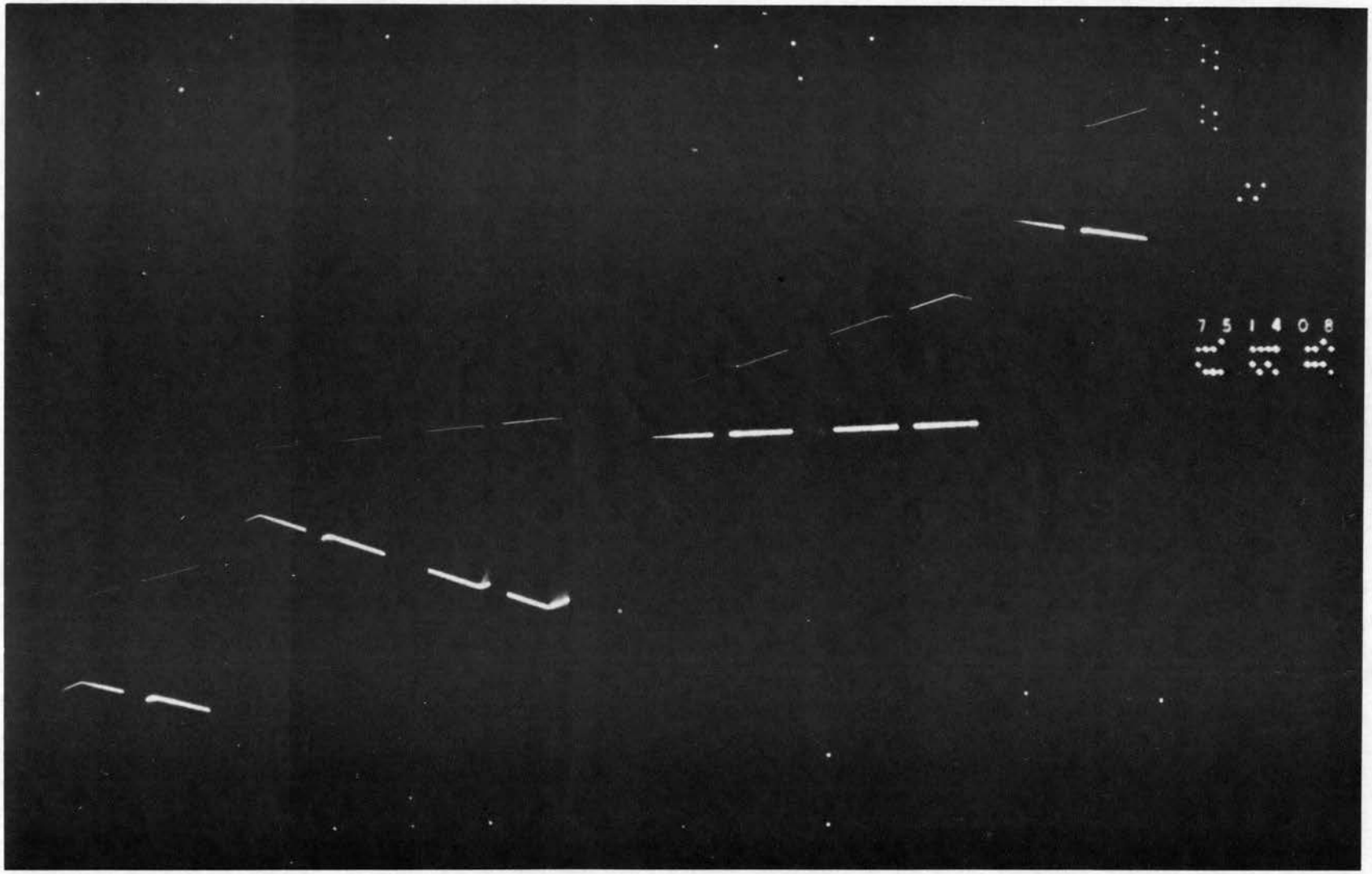

Figure 30. Spark Chamber Photograph of a $\Sigma^{+} \rightarrow p + \pi^{o}$ Event

CHAPTER IV

RESULTS AND THEORETICAL DISCUSSION

Table IV gives a summary of the data analysis and the effect of preliminary cuts on the data. To obtain the best statistical value for the Σ^+ lifetime the maximum likelihood method (13) was used with the expected Σ^+ decay time distribution derived in Appendix A. In addition to sigmas the data includes a contribution from copunctual background events which have a time distribution determined by measurement errors and multiple coulomb scattering in the system. Figure 31 shows a decay time histogram for those events in which the measured ionization ratio differs by two or more standard deviations from the expected ionization ratio. The shape of this distribution can be closely approximated by an exponential $e^{-\Gamma_B t}$ where Γ_B depends on the geometrical cut (coplanarity angle $|\gamma|$) applied. The probability, then, of finding an event with a decay time between t and t + dt is:

$$dN = A\left[(1 - B)\Gamma \exp(-\Gamma t) + B\Gamma_B \exp(-\Gamma_B t)\right]$$

$$= A\, f(\Gamma, t)\, dt ,$$

where

B = background fraction in the data sample,

TABLE IV

DATA ANALYSIS SUMMARY

	Beam Momentum (MeV/c)		
	1106	1134	1164
ZGS Pulses	36,735	28,785	63,103
Pictures Taken (Scanned)	24,685	24,439	43,771
Pictures Measured	3,881	3,849	8,257
PA	3.60×10^8	2.75×10^8	5.84×10^8
$PAQ\overline{B}$	0.83×10^6	0.66×10^6	1.39×10^6
PA/Picture	1.45×10^4	1.12×10^4	1.33×10^4
Fit $\Sigma^+ \rightarrow p\pi^o$ or $n\pi^+$ from Target	1,257	1,409	3,147

The following categories apply only to those events which fit $\Sigma^+ \rightarrow p\pi^o$ or $n\pi^+$ from the target and for which the ionization was measured.

	Combined Data
Ionization Measured	4,394
Ionization Measurement Cut$^+$	4,266
Event Measurement Cut*	3,882
K^+ Lab Angle Cut: $8^o < \theta_K < 36^o$	3,649

$^+$Related to the brightness uniformity of the sparks in a track and defined as the root mean square fractional deviation of the measured spark "widths".

*Removes events with poorly measured fiducials or track coordinates.

Γ_B = background "decay constant",

Γ = Σ^+ decay constant,

and A is determined by the condition

$$A \int_{t_1}^{t_2} f(\Gamma, t) = 1 ,$$

where the limits of integration, t_1 and t_2, are the minimum and maximum time cuts respectively. Evaluating the above integral,

$$A = \frac{1}{(1-B)[\exp(-\Gamma t_1) - \exp(-\Gamma t_2)] + B[\exp(-\Gamma_B t_1) - \exp(-\Gamma_B t_2)]} .$$

The likelihood function is

$$L(\Gamma, B) = \prod_{i=1}^{N} A[(1-B)\Gamma e^{-\Gamma t_i} + B\Gamma_B e^{-\Gamma_B t_i}] .$$

The most probable values, Γ^* and B^*, are given by the solution of the simultaneous equations

$$\left.\frac{\partial L}{\partial \Gamma}\right|_{\Gamma = \Gamma^*} = 0 \qquad \text{and} \qquad \left.\frac{\partial L}{\partial B}\right|_{B = B^*} = 0 .$$

A convenient method of solving these equations is to find the maximum value of the function L (Γ, B) by evaluating it for a series of values of Γ and B. In general, the likelihood function will be close to gaussian; so that L is proportional to

$$\exp[(\Gamma^* - \Gamma)^2/2\sigma_\Gamma^2] \qquad \text{and} \qquad \exp[(B^* - B)^2/2\sigma_B^2] ,$$

where σ_Γ and σ_B are the standard deviations of Γ^* and B^*. The condition $(\Gamma^* - \Gamma) = \sigma$ occurs when $L(\Gamma, B) = e^{-1/2} L(\Gamma^*, B^*) = .60\, L(\Gamma^*, B^*)$ and similiarly for B. Figure 32 shows a plot of the maximum likelihood fitted lifetime versus δ (the fractional deviation of the measured ionization ratio from the expected ionization ratio) for the background fraction equal to zero. Assuming that the background lifetime is independent of δ gives $\tau_B = \frac{1}{\Gamma_B} = (.35 \pm .05) \times 10^{-10}$ sec.

Figure 33 shows a plot of $1/\Gamma$ versus the background fraction for a point corresponding to the maximum value of $L(\Gamma, B)$ and also for points corresponding to one and two standard deviations from the maximum value for events which satisfy the following conditions:

1) the measured ionization ratio is within two standard deviations of the expected ionization ratio (see Figure 29).
2) the measured decay time, t, is greater than 1.0×10^{-10} sec, and less than 4.0×10^{-10} sec.
3) $|\gamma| > 0.14$

The cut on the coplanarity angle, γ, was chosen to reduce the effects of multiple coulomb scattering and measurement error without losing too many events. The shape of the background decay distribution (Figure 31) necessitates the minimum time cut of 1.0×10^{-10} sec. From Figure 33 the most probable value of the Σ^+ decay constant is

$$\Gamma_{\Sigma^+} = (1.43 \pm .18) \times 10^{10} \text{ sec}^{-1}$$

or

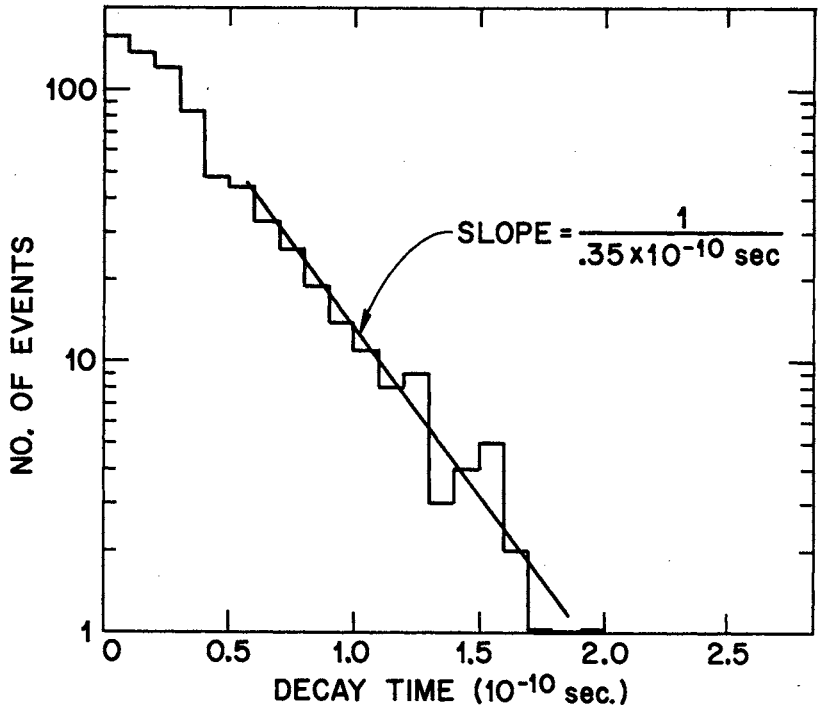

Figure 31. Decay Time Histogram for Nonfit Ionization Events

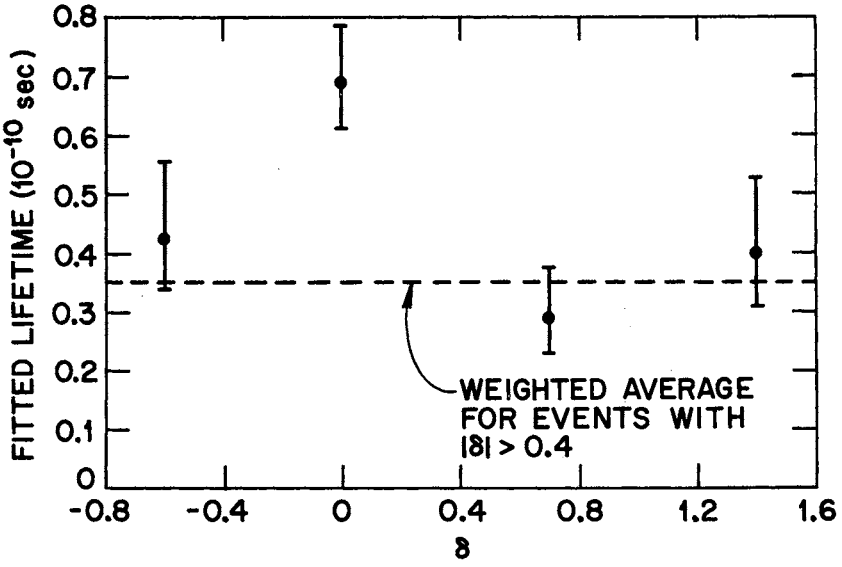

Figure 32. Maximum Likelihood Fitted Lifetime Versus the Fractional Deviation of the Measured Ionization Ratio from the Expected Ionization Ratio

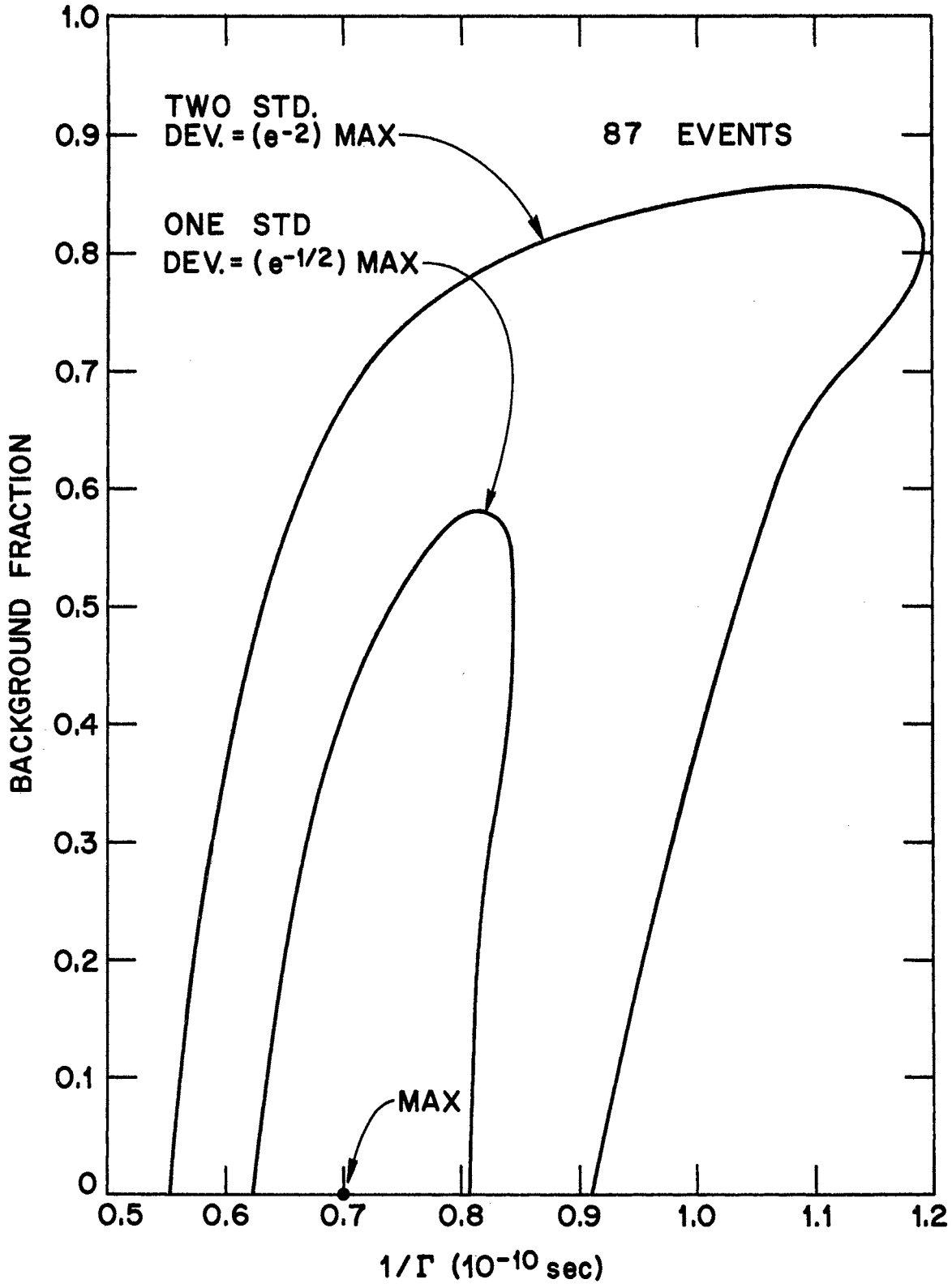

Figure 33. Two Parameter Maximum Likelihood Fit to Sigma Lifetime and Background Fraction

$$\tau_{\Sigma^+} = \frac{1}{\Gamma_{\Sigma^+}} = (.70 \begin{smallmatrix} + .11 \\ - .08 \end{smallmatrix}) \times 10^{-10} \text{ sec.}$$

The result changes by less than 1/2% if the background lifetime is varied over the range $\tau_B = (.3 \text{ to } .4) \times 10^{-10}$ sec. Combining this result with previous Σ^+ lifetime measurements gives

$$\tau_{\Sigma^+}(\text{world}) = (.805 \pm .013) \times 10^{-10} \text{ sec.}$$

The principal features of Σ nonleptonic decay are described in Appendix B, which also gives previously measured values for the sigma decay parameters. The classification of all known weak interactions, including hyperon nonleptonic decay, according to the "universality of strength" hypothesis was first done by Dallaporta (14). Gell-Mann and Rosenfeld (15) have tested this scheme using the experimental rate for $\pi^+ \rightarrow \mu^+ + \nu$ to estimate the hyperon rate for $\Lambda \rightarrow p + \pi^-$ and obtain good agreement with experiment, showing that universality can be applied to nonleptonic decays as well as leptonic decays.

It was suggested by Gell-Mann and Pais (16) that the selection rule $|\Delta I| = 1/2$ (I = total isotopic spin) might be effective in hyperon decays. Appendix C gives the consequences of the $|\Delta I| = 1/2$ rule for Σ nonleptonic decay. Figure 34 shows the vectors $\overline{A}_+$, $\overline{A}_-$, and $\sqrt{2}\,\overline{A}_o$ computed from the January 1969 world data compilation (1). The solution for the direction of the vector $\sqrt{2}\,\overline{A}_o$ is double valued since the sign of the parameter γ_o (Appendix B) is not known. Figure 35 shows the A vectors computed using the measured Σ^+ decay rate from this experiment.

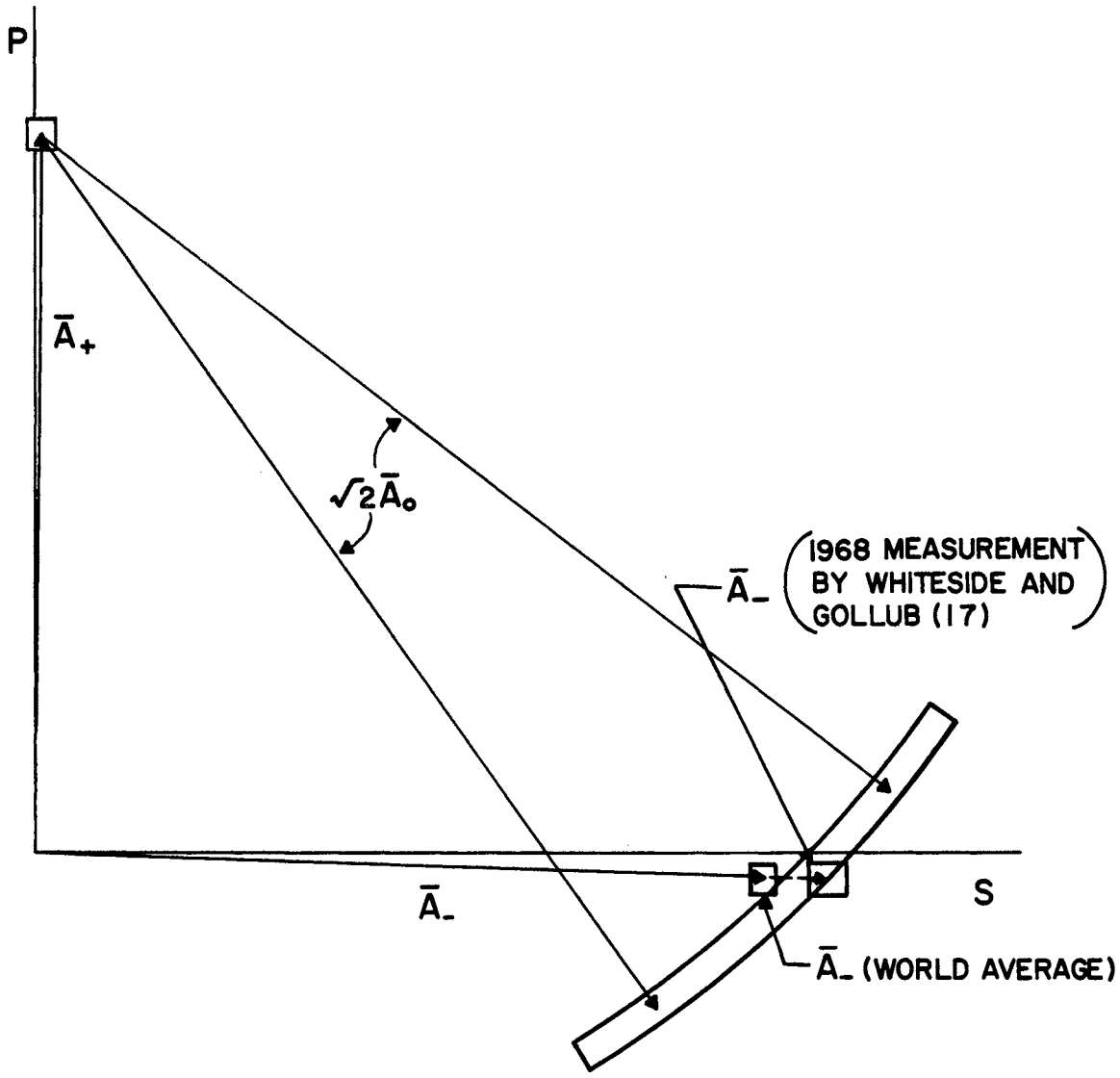

Figure 34. Sigma Decay Amplitudes Computed from the January 1969 World Data Compilation

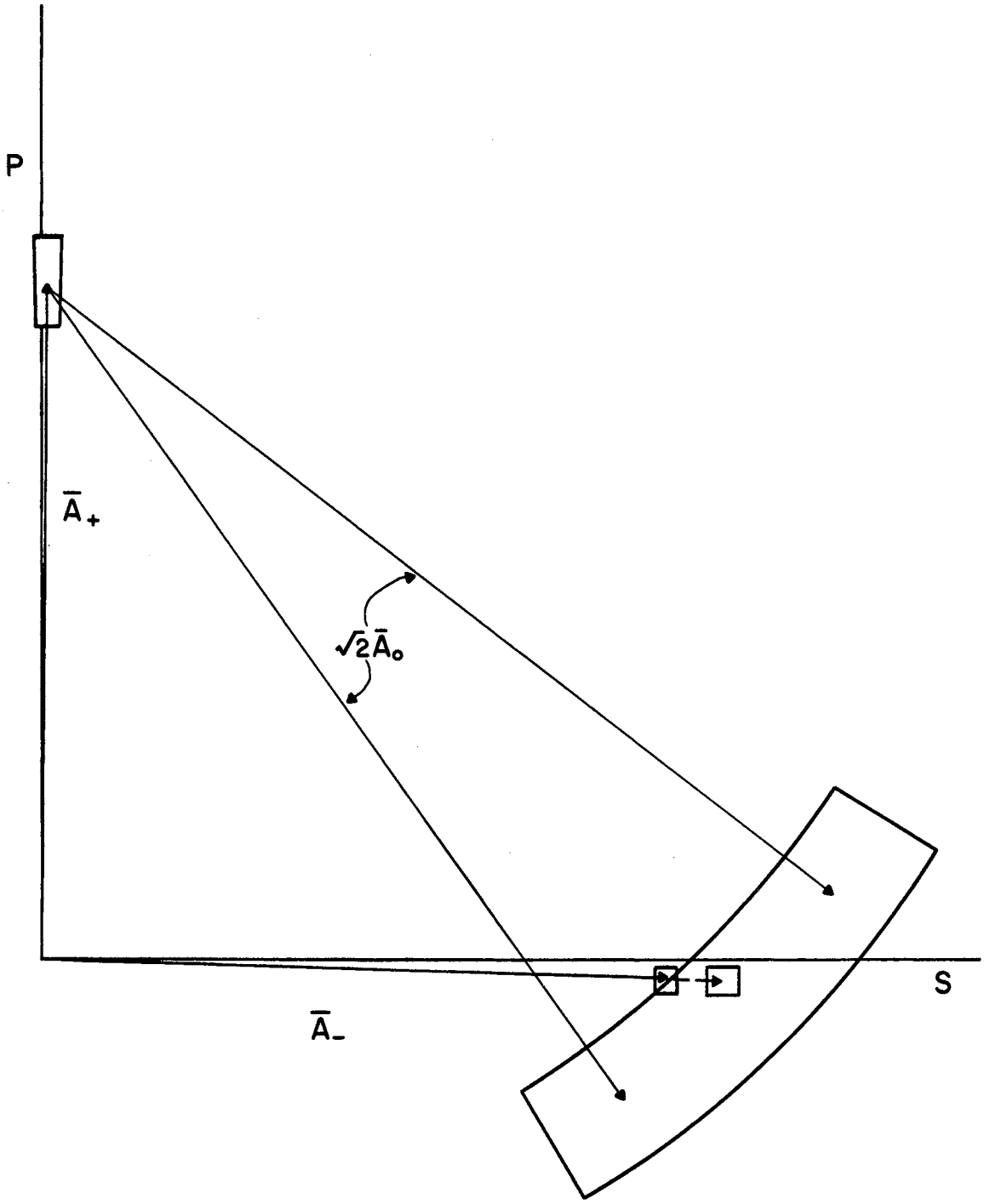

Figure 35. Sigma Decay Amplitudes Computed Using the Measured Σ^+ Decay Rate from this Experiment

Using the current-current model with the assumption of octet dominance (i. e. that the weak interaction currents transform according to the octet representation of SU_3), Gell-Mann (18) has derived the relation

$$2\Xi^- = \Lambda_- + \sqrt{3}\ \Sigma_o^+, \qquad (1)$$

where Ξ^-, Λ_-, and Σ_o^+ are the s-wave amplitudes for the decays $\Xi^- \to \Lambda + \pi^-$, $\Lambda \to p + \pi^-$ and $\Sigma^+ \to p + \pi^o$ respectively. The assumption of octet dominance implies the $|\Delta I| = 1/2$ rule. The fact that equation (1) holds for the p-wave amplitudes as well has not been explained. Using a current algebra (19) approach for s-wave amplitudes only, Sugawara (20) and Suzuki (21) have derived a relation nearly identical to the $|\Delta I| = 1/2$ rule for sigma decay except the sign of the amplitude S_+ is reversed (Appendix C). With the additional assumption of octet dominance they predict $S_+ = 0$, so that their result is indistinguishable from the $|\Delta I| = 1/2$ rule. Attempts to predict the $|\Delta I| = 1/2$ rule for p-waves have been only partially successful (22-26). More recently Good and Nieto (27), starting with the unexplained assumption that the final state reached in the parity-conserving weak decays belongs to the same SU_3 multiplet as the initial state, have obtained the $|\Delta I| = 1/2$ rule as well as $S_+ = 0$, $P_- = 0$, and $S_o/P_o = 1$, which is equivalent to the equality of the amplitudes $|\overline{A}_-|$ and $|\overline{A}_+|$.

REFERENCES

1) N. Barash-Schmidt, A. Bararo-Galtieri, L. Price, A. Rosenfeld, P. Soding, C. Wohl, and M. Roos, Rev. Mod. Phys. 41, 109 (1969).

2) G. Marmer, K. Reibel, D. Schwartz, A. Stevens, T. Romanowski, C. Rush, P. Phillips, E. Swallow, R. Winston, and D. Wolfe, ANL/HEP Report 6801 (Februay 1968).

3) NCR-2 is a registered trademark of National Research Corp., 37 East St., Winchester, Mass. 01890. The material is aluminized 6 μ polyester film which has been crinkled for optimum characteristics as a multilayer reflective insulation.

4) J. Brooks and M. Otavka, Rev. Sci. Instr. 39, 1348 (1968).

5) L. Keller, R. Schluter, and T. White, Nuc. Inst. Meth. 41, 309 (1966).

6) L. Keller, and E. Walschon, Rev. Sci. Instr. 37, 1258 (1966).

7) This camera was a modified version of one described by D. Damouth and O. Haas, "A Pulsed Rapid Film Advance Camera", Technical Report No. 13, Dept. of Physics, University of Michigan (July 1963).

8) Pilot Chemicals Division, New England Nuclear Corp., Watertown, Mass.

9) Autonetics Industrial Products, Los Angeles, California.

10) G. Burleson and C. Smith, ANL/HEP Program Library.

11) R. Royston, ANL/HEP Program Library.

12) V. Galaktionov, F. Yech, and V. Lyubimov, Nucl. Inst. Meth. 33, 353 (1965).

13) M. Bartlett, Phil. Mag. 44, 249 (1953).

14) N. Dallaporta, Nuovo Cimento, 1, 962 (1953)

15) M. Gell-Mann and A. Rosenfeld, Ann. Rev. Nucl. Sci. 7, 407 (1957).

16) M. Gell-Mann and A. Pais, Proceedings of the Glasgow Conference (London: Pergamon Press, 1954).

17) H. Whiteside and J. Gollub, Nuovo Cimento 54A, 537 (1968).

18) M. Gell-Mann, Phys. Rev. Lett. 12, 155 (1964).

19) M. Gell-Mann, Physics 1, 63 (1964).

20) H. Sugawara, Phys. Rev. Lett. 15, 870 (1965).

21) M. Suzuki, Phys. Rev. Lett. 15, 986 (1965).

22) Y. Hara, Y. Nambu, and J. Schlecter, Phys. Rev. Lett. 16, 380 (1966).

23) L. Brown and C. Sommerfeld, Phys. Rev. Lett. 16, 751 (1966).

24) C. Itzykson and M. Jacob, Nuovo Cimento 48A, 655 (1967).

25) Y. Chiu, J. Schlecter, and Y. Ueda, Phys. Rev. 150, 1201 (1967).

26) F. Chan, Phys. Rev. 171, 1593 (1968).

27) M. Good and M. Nieto, Phys. Rev. Lett. 20, 624 (1968).

28) G. Källén, Elementary Particle Physics (Addison-Wesley, 1964), p. 478.

29) G. Takeda, Phys. Rev. 101, 1547 (1956).

30) M. Gell-Mann and A. Rosenfeld, Ann. Rev. Nucl. Sci. 7, 407 (1957).

31) G. Wentzel, Proc. of the Sixth Rochester Conference on High Energy Physics (Interscience, 1956), p. VIII-15.

APPENDIX A

EXPECTED SIGMA TIME DISTRIBUTION

In this experiment the expected Σ^+ time distribution

$$dN = \Gamma e^{-\Gamma t} dt ,$$

where

dN = probability that an event will be found between t and t + dt,

$\Gamma = \Sigma^+$ decay constant,

t = decay time,

must be modified to include the effect of measurement error. It is assumed that for a given event the spread in t due to measurement errors is gaussian with standard deviation σ (this assumption has been tested and shown to be valid with a Monte Carlo program which randomly varied the measured slopes and intercepts according to expected multiple coulomb scattering and known measurement errors). The resultant distribution is

$$dN = \left[A \int_{t'=0}^{\infty} \Gamma e^{-\Gamma t'} e^{-\frac{(t-t')^2}{2\sigma^2}} dt' \right] dt ,$$

where

dN = probability that an event with decay time t will be reconstructed with decay time between t and t + dt,

A = normalization constant.

The above integral cannot be evaluated in closed form; however the normal curve $(1/\sqrt{2\pi}\,\sigma)\exp\left[-(t-t')^2/2\sigma^2\right]$ can be approximated by a triangle function

$$f_T(t') = \frac{1}{2\sigma}\left[1 - \frac{1}{2\sigma}|t-t'|\right] \quad , \quad |t-t'| \leq 2\sigma$$

$$f_T(t') = 0 \quad , \quad |t-t'| > 2\sigma$$

Figure 36 shows the normal curve and the triangle approximation normalized to equal areas. The probability element dN becomes

$$dN = f(t)\,dt = \left[A\int_0^\infty \frac{\Gamma e^{-\Gamma t'}}{2\sigma}\left(1 - \frac{1}{2\sigma}|t-t'|\right)dt'\right] dt \,,$$

where the constant A is determined by the condition

$$\int_{t_1}^{t_2} f(t)\,dt = 1$$

and t_1 and t_2 are the minimum and maximum time cuts made on the data. Because of the absolute value in f (t) this expression cannot be integrated directly but must be divided into regions:

$$df_1 = \frac{\Gamma e^{-\Gamma t'}}{2\sigma}\left[1 - \frac{1}{2\sigma}(t-t')\right] dt' \,, \qquad t > t'$$

and

$$df_2 = \frac{\Gamma e^{-\Gamma t'}}{2\sigma}\left[1 - \frac{1}{2\sigma}(t'-t)\right] dt' \,, \qquad t < t'.$$

This gives for $t \leq 2\sigma$

$$f_A(t) = \int_0^t df_1 + \int_t^{t+2\sigma} df_2 \quad ,$$

and for $t \geq 2\sigma$

$$f_B(t) = \int_{t-2\sigma}^{t} df_1 + \int_t^{t+2\sigma} df_2 \quad .$$

To normalize,

$$C = \frac{1}{\int_{t_1}^{2\sigma} f_A(t)dt + \int_{2\sigma}^{t_2} f_B(t)\,dt}$$

$$= \frac{1}{\left[\frac{C'}{4\Gamma\sigma^2} + \frac{\sinh^2(\Gamma\sigma)}{\Gamma^2\sigma^2}\left(e^{-2\Gamma\sigma} - e^{-\Gamma t_2}\right)\right]} \quad ,$$

where

$$C' = \left[2\Gamma\sigma^2 + 2\sigma - t_1(1+2\Gamma\sigma) + \frac{\Gamma t_1^2}{2} + \frac{1}{\Gamma}\left(e^{-2\Gamma\sigma} - 2\right)\left(e^{-\Gamma t_1} - e^{-2\Gamma\sigma}\right)\right] .$$

Finally

$$dN_A = \frac{C}{4\Gamma\sigma^2}\left[\left(-\Gamma t + 2\Gamma\sigma + 1\right) + \left(e^{-2\Gamma\sigma} - 2\right)e^{-\Gamma t}\right]dt \, , \quad t \leq 2\sigma$$

and

$$dN_B = \frac{C}{\Gamma\sigma^2}\sinh^2(\Gamma\sigma)\,e^{-\Gamma t}\,dt \, , \quad t \geq 2\sigma \, .$$

The probability elements dN_A and dN_B are normalized for a maximum likelihood analysis. Figure 37 shows the expected time distribution

for three values of σ/Γ with $t_1 = 0$ and $t_2 = \infty$. In practice σ will be a function of the event geometry, so that in computing the likelihood function each event will have a different σ.

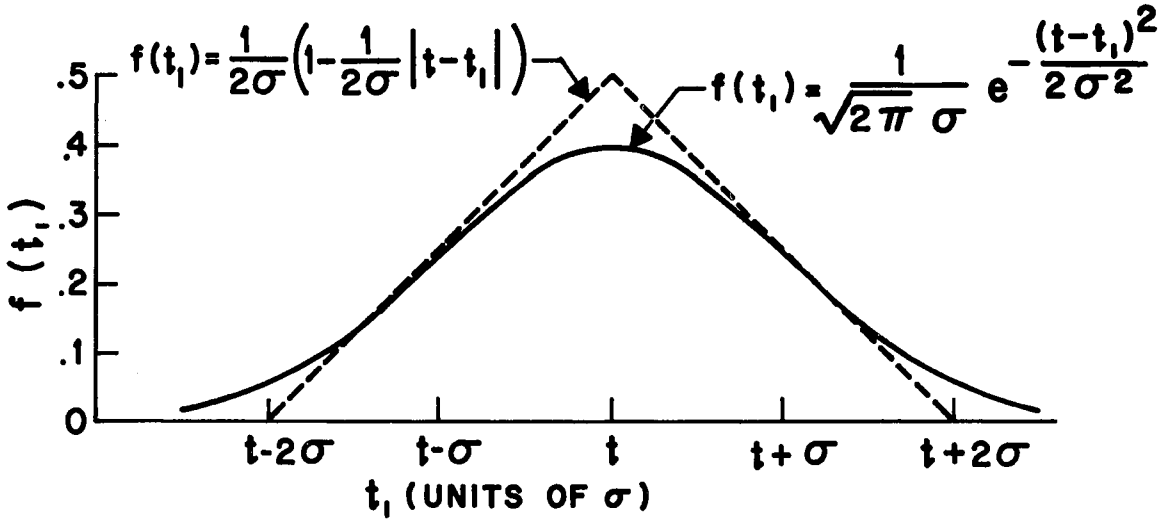

Figure 36. Normal Curve and Triangle Approximation Normalized to Equal Areas

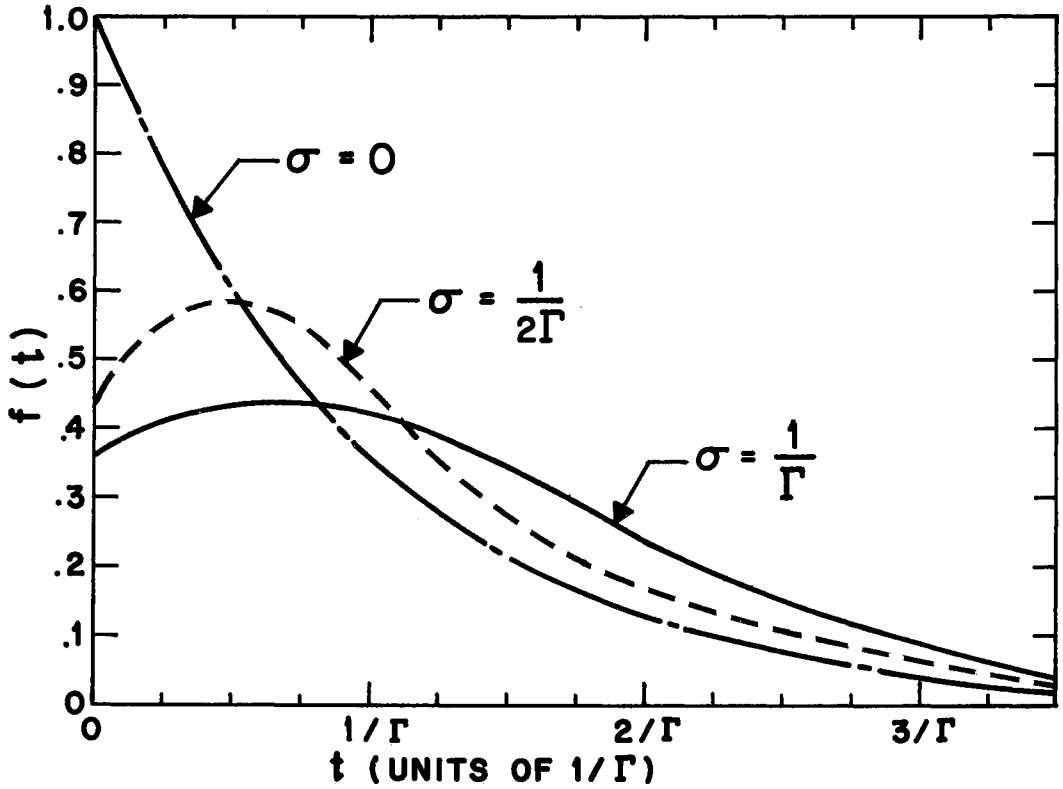

Figure 37. Expected Sigma Decay Time Distribution with Measurement Uncertainty and Multiple Coulomb Scattering Included

APPENDIX B

SIGMA NONLEPTONIC DECAY PARAMETERS

The pion decay of Σ can take place through six channels. There are three charge states $\Sigma^+ \to p\,\pi^0$ or $n\pi^+$ and $\Sigma^- \to n\pi^-$ which are eigenstates of isotopic spin with I = 1/2 and I = 3/2. For each charge state there are also two opposite parity states of orbital angular momentum: the pion-nucleon system with total angular momentum J = 1/2 can be in either an s- or p-wave state with amplitudes S and P respectively. If the Σ is initially polarized, the expectation value of the spin of the final state nucleon is (28)

$$\langle \bar{\sigma} \rangle = \frac{1}{1+\alpha_i \bar{e}_n \cdot \bar{P}} \left[(\alpha_i + \bar{e}_n \cdot \bar{P})\bar{e}_n + \beta_i \bar{e}_n \times \bar{P} + \gamma_i (\bar{e}_n \times \bar{P}) \times \bar{e}_n \right],$$

where

i = +, 0, or - corresponding to the charge of the decay pion,

$$\alpha_i = \frac{2\,\mathrm{Re}(S_i^* P_i)}{|S_i|^2 + |P_i|^2},$$

$$\beta_i = \frac{2\,\mathrm{Im}(S_i^* P_i)}{|S_i|^2 + |P_i|^2},$$

$$\gamma_\lambda = \frac{|S_\lambda|^2 - |P_\lambda|^2}{|S_\lambda|^2 + |P_\lambda|^2} ,$$

$$\alpha_\lambda^2 + \beta_\lambda^2 + \gamma_\lambda^2 = 1 ,$$

$\overline{P}$ = Σ polarization vector,

$\bar{e}_n$ = unit vector along nucleon direction.

The angular distribution of the decay nucleon is

$$W(\theta) = \text{const}\,(1 - \alpha\, \bar{e}_n \cdot \overline{P}),$$

where $\cos\theta = \bar{e}_n \cdot \overline{P}$.

The decay rate for each charge state is

$$\Gamma_\lambda \sim \left[|S_\lambda|^2 + |P_\lambda|^2\right] p_\lambda ,$$

where

p_λ = momentum of decay pion.

The S and P amplitudes are complex numbers. If time reversal invariance is valid, these amplitudes each have a phase equal to that of the pion-nucleon scattering phase shift for the appropriate final state (29). Since the scattering phases are small at the energy for $\Sigma \rightarrow \pi N$ decay, it is a good approximation to take all of the S and P amplitudes to be real (30). Table V gives a compilation of the most recent measured values for the Σ decay parameters (1).

The asymmetry parameter α_o is consistent with unity, corresponding to a maximal parity violation in $\Sigma^+ \rightarrow p\pi^o$, whereas the other two

charge states show little or no parity violation. The signs of γ_+ and γ_- show that $\Sigma^+ \to n\pi^+$ is predominantly p-wave while $\Sigma^- \to n\pi^-$ is predominantly s-wave.

TABLE V

MEASURED Σ DECAY PARAMETERS

	a_i	ϕ_i	β_i (derived)	γ_i (derived)	Γ_i (10^{10} sec^{-1})*
$\Sigma^+ \to p\pi^o$	-.95 ± .07				.652 ± .011
$\Sigma^+ \to n\pi^+$	.018 ± .039	(161 ± 21)°	.31 ± .33	-.95	.583 ± .010
$\Sigma^- \to n\pi^-$	-.06 ± .05	(4 ± 17)°	.07 ± .30	1.0	.610 ± .022

$$\beta_i = \sqrt{1 - \alpha_i^2}$$

$$\gamma_i = \sqrt{1 - \alpha_i^2}$$

$$i \equiv (o, +, -)$$

*The two partial Σ^+ decay rates are computed from the measured total Σ^+ decay rate, (1.23 ± .02) x 10^{10} sec^{-1} and the measured branching ratio (47.2 ± 1.5)%, for the $n\pi^+$ decay.

APPENDIX C

THE $|\Delta I| = 1/2$ RULE FOR SIGMA NONLEPTONIC DECAY

The consequences of the $|\Delta I| = 1/2$ rule are most easily obtained by using the spurion formalism first proposed by Wentzel (31). The final πN state can have $I = 1/2$ or $3/2$ while the initial Σ has $I = 1$. To account for the possible changes $|\Delta I| = 1/2$, $3/2$, or $5/2$ imagine that the Σ absorbs a "spurion", s^o, whose sole property is that it has $I = 1/2$, $3/2$, or $5/2$ and $I_z = -1/2$. The spurion causes isospin to be conserved but has no effect on the kinematics of the decay. Using Clebsch-Gordan coefficients with the notation $|I, I_z\rangle$,

$$|n\pi^+\rangle = \sqrt{1/3}\,|3/2, 1/2\rangle + \sqrt{2/3}\,|1/2, 1/2\rangle ,$$

$$|p\pi^o\rangle = \sqrt{2/3}\,|3/2, 1/2\rangle - \sqrt{1/3}\,|1/2, 1/2\rangle ,$$

$$|n\pi^-\rangle = |3/2, -3/2\rangle .$$

and

$$\left.\begin{aligned} |\Sigma^+ s^o\rangle &= \sqrt{1/3}\,|3/2, 1/2\rangle + \sqrt{2/3}\,|1/2, 1/2\rangle , \\ |\Sigma^- s^o\rangle &= |3/2, -3/2\rangle , \end{aligned}\right\} \Delta I = 1/2$$

Also

$$\left.\begin{aligned} |\Sigma^+ s^o\rangle &= \sqrt{3/10}\,|5/2, 1/2\rangle - \sqrt{8/15}\,|3/2, 1/2\rangle + \sqrt{1/16}\,|1/2, 1/2\rangle , \\ |\Sigma^- s^o\rangle &= \sqrt{3/5}\,|5/2, -3/2\rangle + \sqrt{2/5}\,|3/2, -3/2\rangle , \end{aligned}\right\} \Delta I = 3/2$$

and

$$\left.\begin{aligned} |\Sigma^+ s^o\rangle &= \tfrac{2\sqrt{3}}{6}\left|\tfrac{7}{2},\tfrac{1}{2}\right\rangle - \tfrac{3}{\sqrt{30}}\left|\tfrac{5}{2},\tfrac{1}{2}\right\rangle + \sqrt{\tfrac{1}{5}}\left|\tfrac{3}{2},\tfrac{1}{2}\right\rangle , \\ |\Sigma^- s^o\rangle &= \sqrt{\tfrac{1}{6}}\left|\tfrac{7}{2},-\tfrac{3}{2}\right\rangle + \tfrac{4}{\sqrt{15}}\left|\tfrac{5}{2},-\tfrac{3}{2}\right\rangle + \sqrt{\tfrac{2}{5}}\left|\tfrac{3}{2},-\tfrac{3}{2}\right\rangle . \end{aligned}\right\} \Delta I = 5/2$$

The amplitudes for the three nonleptonic decays are

$$A_+ = \sum_{\Delta I = 1/2, 3/2, 5/2} \langle n\pi^+ | T | \Sigma^+ s^o \rangle ,$$

$$A_o = \sum_{\Delta I = 1/2, 3/2, 5/2} \langle p\pi^o | T | \Sigma^+ s^o \rangle ,$$

$$A_- = \sum_{\Delta I = 1/2, 3/2, 5/2} \langle n\pi^- | T | \Sigma^- s^o \rangle ,$$

where the subscript on A is taken from the charge of the decay pion and T is a transition operator joining the states. Using the relations

$$\langle I, I_z | T | I', I_z' \rangle = \delta_{II'} \delta_{|I_z||I_z'|} \; T(2\Delta I, 2I)$$

the amplitudes are

$$A_+ = \tfrac{2}{3} T(1,1) + \tfrac{1}{3} T(1,3) + \tfrac{1}{3} T(3,1) - \tfrac{2}{3}\sqrt{\tfrac{2}{5}}\, T(3,3) + \sqrt{\tfrac{1}{15}}\, T(5,3),$$

$$A_o = -\sqrt{\tfrac{2}{3}}\, T(1,1) + \sqrt{\tfrac{2}{3}}\, T(1,3) - \tfrac{1}{3\sqrt{2}} T(3,1) - \tfrac{4}{3\sqrt{15}} T(3,3) + \sqrt{\tfrac{2}{15}}\, T(5,3),$$

$$A_- = T(1,3) + \sqrt{\tfrac{2}{5}}\, T(3,3) + \sqrt{\tfrac{1}{15}}\, T(5,3) .$$

Combining,

$$A_+ + \sqrt{2}\, A_o - A_- = -3\sqrt{2/5}\, T(3,3) + 2/\sqrt{15}\, T(5,3) .$$

If only $|\Delta I| = 1/2$ transitions are allowed,

$$A_+ + \sqrt{2}\, A_o = A_-$$

This relation holds separately for the s- and p-wave amplitudes; so that the amplitudes A can be considered vectors in an S-P plane, $\overline{A} = (S, P)$, which implies that $\overline{A}_+, \sqrt{2}\,\overline{A}_o$, and $\overline{A}_-$ should form a triangle in the plane.

VITA

Lewis Porter Keller

Candidate for the Degree of

Doctor of Philosophy

Thesis: SPARK CHAMBER MEASUREMENT OF THE Σ^+ LIFETIME

Major Field: Physics

Biographical:

Personal Data: Born in Valparaiso, Indiana, July 25, 1938, the son of Mr. and Mrs. Charles Keller

Education: Graduated from Valparaiso High School, Valparaiso, Indiana in 1956; received Bachelor of Science degree from Valparaiso University in May, 1960; received Master of Science degree from Oklahoma State University in August, 1962, with a major in Physics; completed requirements for the Doctor of Philosophy degree at Oklahoma State University in May, 1969.

Professional Experience: Resident Student Associate, Argonne National Laboratory, summers of 1961 and 1963, currently Research Associate, Argonne National Laboratory.

Professional Organization: American Physical Society

Publications:

1) With R. Schluter, T. White, and G. Burleson, "Precise Track Measurements in a Wide Gap Spark Chamber," IEEE Trans. NS-12, No. 4, 19 (1965).

2) With R. Schluter, T. White, and D. Worcester, "Wide Gap Spark Chamber: Track Sharpening in Intense Beam Tests," Bull. Am. Phys. Soc. 10, 1123(1965).

3) With R. Schluter and T. White, "Operational Characteristics of a Wide Gap Spark Chamber," Nucl. Inst. Methods 41, 309 (1966).

4) With E. Walschon, "Simple Marx High Voltage Pulse Generator for Wide Gap Spark Chambers," Rev. Sci. Inst. 37, No. 9, 1258 (1966).

5) With E. Hoffman, S. Berezin, G. Burleson, R. Schluter, and T. White, "Spark Chamber Measurement of the Σ^+ Lifetime," Bull. Am. Phys. Soc. 14, 94 (1969).

6) With E. Hoffman, S. Berezin, G. Burleson, R. Schluter, and T. White, "Measurement of Sigma Polarization for the Reaction $\pi^+ p \rightarrow \Sigma^+ K^+$ Using Wide Gap Spark Chambers," Bull. Am. Phys. Soc. 14, 94 (1969).